Supplementary material

Batch and column adsorption of cations, oxyanions and dyes from water on a magnetite modified cellulose-based membrane

Jovana Perendija[a], Zlate S. Veličković[b], Ilija Cvijetić[c], Jelena D. Rusmirović[d,e], Vukašin Ugrinović[d], , Aleksandar D. Marinković[f], Antonije Onjia[f]

[a]*SI Institute of Chemistry, Technology and Metallurgy-National Institute, Center of Ecology and Technoeconomics, Njegoševa 12, 11001 Belgrade, Serbia; Tel. +38160 6805 804, email: j.nikolic.ihtm@tesla.rcub.bg.ac.rs*

[b]*Military Academy, University of Defense, Veljka Lukića Kurjaka 33, 11000 Belgrade, Serbia; Tel. +38165 2429 431, email: zlatevel@yahoo.com (Z. S. Veličković)*

[c]*Innovation Center, Faculty of Chemistry, University of Belgrade, Studentski trg 12, 11000 Belgrade, Serbia*

[d]*Innovation Center, Faculty of Technology and Metallurgy, Karnegijeva 4, 11120 Belgrade, Serbia;*

[e]*Military Technical Institute, Ratka Resanovića 1, Belgrade 11000, Serbia, e-mail: jrusmirovic@tmf.bg.ac.rs*

[f]*Faculty of Technology and Metallurgy, University of Belgrade, Karnegijeva 4, 11060 Belgrade, Serbia; Tel. +381 3303 750, email: marinko@tmf.bg.ac.rs (A. D. Marinković)*

List of symbols

Q_M	material density
Q_P	sample density
m_M	weight of the dry sample
m_w	weight of the wet sample
V	volume of the wet sample
q_s	the density of ethanol
C_e	equilibrium ion concentration in the solution (mg dm^{-3})
q_e	adsorbed amount of ions at equilibrium (mg g^{-1})
q_m	maximum adsorption capacity (mg g^{-1})
K_L	Langmuir constant
K_F	Freundlich constant
n^{-1}	Freundlich adsorption intensity parameter
R_L	dimensionless equilibrium parameter
C_i	initial metal ion concentration (mg dm^{-3})
B	Dubinine-Radushkevich (D-R) constant (mol^2 kJ^{-2})
R	universal gas constant (J mol^{-1} K^{-1})
T	temperature (K)
A	Temkin isotherm equilibrium binding constant (dm^3 g^{-1})
b	Temkin isotherm constant
ΔG^0	Gibbs free energy (KJ mol^{-1})
ΔH^0	enthalpy change of adsorption (KJ mol^{-1})
ΔS^0	entropy change of adsorption (KJ mol^{-1})
k_1	pseudo-first rate constant (min^{-1})
q_t	adsorption capacity at time t (mg g^{-1})
t	time (min)
k_2	the second-order rate constant (g mg^{-1} min^{-1})
h_2	initial sorption rate at t→0 (mg g^{-1} min^{-1})
a	initial ions adsorption rate (mg g^{-1} min^{-1})
b	Elovich constant (g mg^{-1}).
R_E	approaching equilibrium parameter based on Elovich equation
k_i	intraparticle diffusion rate constant (mg g^{-1} min$^{1/2}$)
C_{BL}	constant related to the thickness of the boundary layer
K	rate constant of adsorption (min^{-1})
r	initial radius of the reacting particle
α	fractional completion of reactions at time t
D	diffusion coefficient of the migrating species
k_{DW}	Dunwald-Wagner isothermal reaction constant
D_s	intraparticle diffusion coefficient

r	radial position
R	distance from the center of the adsorbent particle during adsorption
C_0	initial concentration of heavy metal (mol dm^{-3})
C_t	concentration of heavy metal at time t (mol dm^{-3})
t	flow time (min)
Θ	time required for 50 % breakthrough (min)
K_{YN}	the Yoon-Nelson rate constant (min^{-1})
Z	bed depth of column (cm)
N_0	maximum dye uptake capacity per unit volume of adsorbent column(mg dm^{-3})
U_0	linear velocity of influent dye solution (cm min^{-1})
K_{AB}	the kinetic constant (dm^3 mg^{-1} min^{-1})
q_0	the equilibrium uptake per g of the adsorbent (mg g^{-1})
m	the amount of the adsorbent in the column (g)
a	parameter from the modified dose-response model
b	parameter from the modified dose-response model
C	sorbate concentration in the effluent (mmol·dm^{-3})
C_0	sorbate concentration in the feed solutions (mmol· dm^{-3})
U_0	linear flow rate (cm·min^{-1})
Z	the bed column depth (cm)
t	adsorption time (min)
β	kinetic coefficient of the external mass transfer (min^{-1})
N_0	volumetric saturation capacity of the adsorbent (mmol· dm^{-3})
n	Freundlich constant
C_b	concentration at breakthrough (mmol· dm^{-3})
k_T	mass-transfer rate coefficient (min^{-1})
υ	migration velocity of the concentration fronts in the bed (cm·min^{-1})
V	volume of the permeate (dm^3)
A	effective membrane area (m^2)
t	running time (h)
C_p	concentration of permeate
C_f	concentration of feed solution
ε	adsorption energy of the receptor site
μ	chemical potential of the adsorbed state determined from the Gibbs free energy
β	Boltzmann factor
Q	adsorption capacity
n	number of ions per site
N_M	density of receptor site
c	heavy metal ion/oxyanion equilibrium concentration

2. Experimental part

2.1 Chemicals and materials

All the chemicals used in this study were of analytical grade and used as received. Waste cellulosic materials was collected from Belgrade landfill (waste undershirt). The following chemicals were supplied from Sigma Aldrich: diethylenetriaminepenta-acetic acid (DTPA), pyridine, acetic anhydride, diethyl ether,sulfuric acid, hydrogen peroxide, sodium hydroxide, dimethylacetamide (DMAc), 3-aminopropyltriethoxysilane (APTES), absolute ethanol, dimethyl sulfoxide (DMSO), iron(II) sulfate heptahydrate ($FeSO_4 \cdot 7H_2O$), potassium nitrate (KNO_3), potassium hydroxide (KOH). Diatomaceous earth was also supplied by Sigma Aldrich. The Ni^{2+}, Pb^{2+}, Cr(VI) and As(V) stock solutions were prepared with deionized water (DW), resistivity 18 MΩ cm, using standards of Lead, Nickel, Chromium and Arsenic, 1000 mg dm^{-3} (Sigma), respectively. The dyes (Methyl Orange - MO, Methylene Blue - MB, Reactive Black 5 – RB5 and Direct Red 80 – DR80) were purchased from Merck. Adjustment of pH was accomplished with 0.1 M NaOH and 0.1 M HNO_3 (Sigma Aldrich).

2.2 Synthesis of dianhydride of diethylenetriaminepenta-acetic acid

Bis(2-(2,6-dioxomorpholino)ethyl)glycine (Diethylenetriaminepenta-acetic acid dianhydride; DTPA) was prepared by the following procedure: In a three-necked flask equipped with thermometer/thermocouple, inert gas inlet tube and addition funnel, a solution of DTPA (0.033 mol) in pyridine was reacted with acetic anhydride (50 cm^3), added for 3 minute, under N_2 stream. Furthermore, the mixture was heated at 65°C and stirred for 24 h. Obtained reaction product was cooled and filtered under N_2, then was washed with acetic anhydride (Ac_2O) and diethyl ether and dried under vacuum to give DTPA dianhydride (D'Halluin et al. 2017).

2.3 Pre-treatment of cellulose fibres (Cell)

The purification treatment of cellulose fibres was carried out in order to remove impurities, increase fibres porosity and to obtain quantitatively larger number of available surface functional groups, mainly hydroxyl. Different pre-treatments of cellulose and diatomite were applied using acid (1 and 5 % H_2SO_4), piranha solution (1-5 % H_2SO_4 and 1-5 % H_2O_2), NaOH (1-5 %), solvent/salt system (DMSO and DMAc with 5% LiCl) or their combination at different temperatures (20-60 ºC). Optimal procedure, after mechanical and microscopy examination, was established as follow: 10 g of Cell swelled in 0.5 % (w/v) sodium hydroxide solution at 25 °C for 1 h and then washed with deionized water and ethanol for several times. The obtained fibres were soaked in 100 cm^3 DMAc/LiCl (5 % LiCl) at 25 °C for 6 h in order to remove impurity, cause material swelling, i.e. to increase surface reactivity. Finally, material was washed with plenty of water, and dried using freeze/drying technique (freezing at –30 °C for 24 h, followed by drying at –50 °C/0.05 mbar for 24 h, and at–70°C/0.01 mbar for 1h).

2.4 Procedure for preparation of amino-functionalized Cell fibres (Cell-NH$_2$) and diatomaceous earth (D-APTES)

The functionalization with 3-aminopropyltriethoxysilane (APTES) surface modifier/-coupling agent is an effective method for the modification of the physical and chemical properties of the treated fibres. After purification and activation treatments,10 g of Cell fibres were modified using different quantity of APTES in absolute toluol (100 cm^3): 2.5 %, 5.0 %, 7.5 % and 10.0 %. Optimal procedure was established at 5 % (v/v) APTES with respect to introduced amino group. The silanization was carried out for 10 h, and after 96 % ethanol (5 cm^{-3}) was added drop-wise to the reaction mixture. After cooling the obtained product was filtered, washed with toluol and ethanol, and dried under vacuum at 50 ºC/2000 Pa for 6 h.

In an analogous manner was produced D-APTES: 0.5 g of diatomite was suspended in 15 cm^{-3} of dry toluene in a three-necked 50 cm^3 round-bottomed flask, which was fitted with a thermometer, a reflux condenser and a N$_2$ gas inlet tube. Then, 0.5 cm^3 of APTES was added and the reaction mixture was heated at 70 °C for 10 h. Obtained mixture was cooled, filtered and washed with toluene (20 cm^3), ethanol (20 cm^3) and dried under vacuum (50 ºC/2000 Pa) and stored in a desiccator.

2.8 Characterization of adsorbents

2.8.1 Mechanical properties

The tensile tests of the cellulose membranes in dry condition were performed, using a Universal Testing Machine, Shimadzu Autograph AG-X plus (Japan), with a load cell of 1 kN. The gauge length was 30 mm, thickness was 3 mm and width on 4.5 mm. Tensile strength tests were conducted with a constant cross head speed of 2 mm/min.

2.8.2 Thermogravimetric Analysis (TGA)

In order to determine the thermal stability of the Cell, Cell-NH$_2$, Cell-DTPA fibres and Cell-MG hybrid membrane under study, their thermal properties were evaluated by thermogravimetric analysis (TGA). TGA test was performed by using TA Instruments, SDT-Q600. The flow rate of nitrogen was 100 cm^3/min and the heat rate was 10 °C/min. The samples weighed at around 5 mg. The samples were heated from the temperature of 24°C to above 800 °C.

2.8.3 FTIR spectroscopy

Fourier-Transfer Infrared Spectroscopy analysis (FTIR) of samples was performed using Thermo Scientific Nicolet 6700 spectrometer in the attenuated total reflectance (ATR) mode. The range of wavenumber was 3500 - 500 cm^{-1}.

2.8.4 Raman spectroscopy

Raman spectra were collected with aXploRA Raman spectrometer, which employed laser at 532 nm (maximum output power 20-25 mW).

2.8.5 XRD analysis

Phase and structural analysis of adsorbents were determined by the X-ray diffraction (XRD) (Bruker D8 ADVANCE).

2.8.6 Surface Morphology analysis

The surface morphology of the samples was examined using a Tescan Mira3 XMU field emission scanning electron microscope (FE-SEM), operated at 20 kV.

2.8.7 Image analysis

Software Image-Pro Plus 6.0 was used to obtain the statistical data of the fibre diameters and spacing porosity of the Cell and Cell-MG membranes.

2.8.8 Porosity determination

To evaluate porosity of materials, the procedure earlier described elsewhere was used. An amount (100 mg) of each sample was completely wetted with ethanol in a glass test tube in order to fill all inner pores with this solvent. Material and sample density, Q_M and Q_P, was calculated from the Eq.S1 and Eq. S2, based on the experimentally determined difference in weight and volume between the dry and wet sample.

$$Q_M = \frac{m_M}{V - \frac{m_W - m_M}{q_S}} \tag{S1}$$

$$Q_P = \frac{m_M}{V} \tag{S2}$$

Where m_M represents the weight of the dry sample; m_w represents the weight of the wet sample; V represents the volume of the wet sample and q_s represents the density of ethanol.
The sample porosity can be calculated from the material density and the sample density using the Eq. S3

$$\varepsilon_P = \frac{Q_M - Q_P}{Q_P} = 1 - \frac{Q_P}{Q_M} \tag{S3}$$

where Q_P presents sample density and Q_M presents material density.

2.8.9 Amino group and carboxylic content determination

Quantification of the available amino group was determined *via* "back" (indirect) titration. 10 mg of cellulose-based adsorbents were placed in 10 cm^3 0.01 mol dm^{-3} HCl and ultrasonicated for 15 min. Materials were filtered, and 10 cm^3 of supernatant was titrated with a standard solution of 0.01 mol dm^{-3} KOH in the presence of methyl orange indicator. The acid value (*AV*) was determined by titration of the sample solution in mixture of isopropyl alcohol/water (50%) with standard (0.5 N) alcoholic KOH solution (ASTM D3644).

2.9 Batch adsorption experiments

The concentrations of ions (Pb^{2+}, Ni^{2+}, Cr(VI) and As(V)) were measured by atomic absorption spectrometry (AAS) using a Perkin Elmer PinAAcle 900T. In order to evaluate the performance of the Cell-COOH and Cell-MG hybrid membrane, batch adsorption experiments were conducted by equilibration of Pb^{2+}, Ni^{2+}, Cr(VI) and As(V) adsorbate solution under magnetic stirring. Adsorption experiments were performed by addition of 1, 2, 3, 4, 5, 7.5 and 10 mg of adsorbent in a vials of 8 cm^3 containing 12.2, 12.5, 13.05 and 7.55 mg dm^{-3} of standard solutions of Pb^{2+}, Ni^{2+}, Cr(VI) and As(V) ions, respectively. The optimal pH-value was defined at 6. Adsorption equilibrium and thermodynamic parameters were evaluated at three temperatures (25, 35 and 45 °C). The adsorption kinetic was studied by varying the contact time: 1, 5, 15, 30, 45, 60, 75, 90 minutes and 24 h at C_i = 12.2, 12.5, 13.05 and 7.55 mg dm^{-3} for Pb^{2+}, Ni^{2+}, Cr(VI) and As(V) respectively, pH_i=6 at 25, 35 and 45 °C. After adsorption, the sample solutions were filtered through a nylon membrane syringe filter (pore size 0.22 µm). The Pb^{2+}, Ni^{2+}, Cr(VI) and As(V) uptake of adsorbent adsorbed per mass unit of the adsorbent were calculated from the Eq. S5 (Ren et al. 2017):

$$q = \frac{(c_i - c_f)}{m} V \tag{S4}$$

where q is the adsorption capacity in mg g^{-1}, C_i and C_f are the initial and final concentrations of ions in the solution in mg dm^{-3}, V is the volume of solution in dm^{-3}, and m is the mass of the adsorbent in g. Adsorption isotherms are determined as the dependence of q, mg g^{-1} from equilibrium concentration C_e, mg dm^{-3} based on the calculated values of q. Calculated values were fitted to four models of adsorption isotherms (Langmuir, Freundlich, Temkin and Dubinin-Radushkevich models).

2.9.1 Regeneration study

To evaluate the regeneration capabilities, i.e. desorption capability, after adsorption experiments and washing with DI, wet adsorbents (m/V=100 mg dm^{-3}) were re-dispersed in 20 cm^3 of regenerant. Different solution: NaOH (0.2 or 0.5 mol dm^{-3}), NaCl (0.2 or 0.5 mol dm^{-3}) or citrate (0.01 mol dm^{-3}) or their combination was used for pollutant elution. Also, other regenerator Na_2CO_3, KOH, EDTA, *conc*. HCl and sulfuric acid, citric and oxalic acid were used with lower success. The amount of desorbed Pb^{2+}, Ni^{2+}, Cr(VI) and As(V) was measured after magnetic mixing for 3 h in a batch system. Five consecutive adsorption/desorption cycles were performed in triplicate. The collected effluent water was analyzed using atomic absorption spectrometry (AAS) using a Perkin Elmer PinAAcle 900T.

2.9.2 Membrane performance

Batch adsorption experiments for dyes were conducted in glass vials in a water bath shaker (25°C, 200 rpm). Each vial contained 40cm^3 MO, MB, RB5 and DR80 solution and 5 mg adsorbent. The pH of the solution was adjusted by adding 0.1 M HCl or NaOH aqueous solutions. At predetermined time intervals, approximately 3 cm^{-3} of dye solution were used for UV/Vis measurements and afterwards returned into the vial. This was repeated until equilibrium was reached. The dye removal efficiencies of the Cell-MG hybrid membrane towards MO, MB, RB5 and DR80 dyes were investigated for 90min (C_i[MO] =27 mg dm^{-3}, pH 6; C_i[MB] = 30 mg dm^{-3}, pH 7.5; C_i[RB5] = 25 mg dm^{-3} and C_i[DR80] = 36 mg dm^{-3}, pH 6). UV-spectrophotometer (SHIMADZU, UV-1700) was used to measure the concentration of dyes in solution. Flux was measured using a cross-flow filtration system presented in

Figure S1. For the pH measurements a laboratory pH meter, InoLab Cond 730 precision conductivity meter (WTW GmbH), with an accuracy of ± 0.01 pH units, was used.

2.9.3 Adsorption studies with industrial wastewater

A contaminated mining wastewater, collected at location of eastern Serbia, was additionally spiked or diluted in order to make different levels of Pb^{2+}, Ni^{2+}, $Cr(VI)$ and $As(V)$ to obatine concentration given in Table S12, which mimic the real mining wastewater sample. The batch and flow adsorption studies were subsequently conducted to evaluate Cell-MG adsorbent performance. The collected effluent water was analyzed byatomic absorption spectrometry (AAS) using a Perkin Elmer PinAAcle 900T.

2.10 Bed column experiments

Cell-MG hybrid adsorbent was carefully cut and packed into a glass column to achieve optimal system packing. A glass tube of 0.5×10 cm (d×H) with a sintered filter and PTFE valve packed with Cell-MG was used to conduct the flow-through column experiment with a down-flow design. Sand was added to the top of the column bed after pre-treatment to prevent an even flow distribution. A column adapter was attached to the top of the column to allow PTFE tubing to be fitted into the column. Prior to the column being attached, the feeding solution (DW) was pumped through the tubing to remove any impurities from the rig. After the addition of DW, a vacuum was applied to remove air bubbles trapped during inflow of feeding solution. The effluent samples were collected at a predetermined period of time and the concentration of arsenic in the effluent was determined using AAS technique. The mass of adsorbent in the column was 430.0 mg. The solutions of ions (C_i = 6.2, 6.1, 6.2 and 5.0 mg dm^{-3} for Pb^{2+}, Ni^{2+}, $Cr(VI)$ and $As(V)$) of known concentration was adjusted to pH 6 and passed through the column at 0.5, 1.0 and 1.5 cm^3 min^{-1} flow rate, respectively. Samples were collected at regular intervals and the concentrations of heavy metals in the effluent were analysed using a AAS spectrophotometer (Perkin Elmer PinAAcle 900T).

The flow rate Q, empty bed volume (EBV), and pH-value were adjusted to obtain optimal empty bed contact time ($EBCT$). The flow rate of feed solution was varied at Q= 0.5, 1.0 and 1.5cm^3 min^{-1}. All experiments were performed at 25 °C. The feed water was allowed to pass through the hybrid adsorbent bed using peristaltic pump Ismatec. Residence time $EBCT$ was calculated according to: $EBCT$ = H/γ, where H is bed depth (cm) and γ is the linear flow rate (cm^3 cm^{-2} s^{-1}). The breakthrough point (BP) was designated as the feed volume supplied to a column up to maximum permissible limit (MPL) to heavy metals. $BP=C_{MPL}/C_i$, BP for Pb^{2+}, Ni^{2+}, $Cr(VI)$ and $As(V)$ is 0.008, 0.0016, 0,003 and 0,0013 respectively.

2.11 Response surface methodology (RSM): experimental design of adsorbent preparation

The influence of membrane synthesis parameters (Table S1) and adsorption parameters (Table S2) was performed using response surface methodology (RSM) (Witek-Krowiak et al. 2014; Rout et al. 2015; Jafari et al. 2015; Iqbal et al. 2016). D-optimum design, with 2 (Table S1) or 3 (Table S2) Numerical Factors or that minimizes variances associated with the estimates of coefficients for the model, is used. The coded and operational values of the selected variables are shown in Table S1 and S2, together with the experimental design, which included 16 experimental runs cycles with three repetitions at the central point. Each

experiment (except the center point) is performed in duplicate. The output variable were COOH group content in Cell-COOH membrane and capacity of Cell-MG with respect to Ni^{2+}, $q_{e[Ni^{2+}]}$ (Table S1 and S2, respectively), and capacity of Cell-MG with respect to Pb^{2+} (Table S16). Experimental data were fitted with a second-order polynomial equation and the coefficients of the response function and their statistical significance were evaluated by the least-squares method using commercial software Design-Expert, Software Version 9 (Stat-Ease, Inc. 2021 E. Hennepin Ave. Suite 480 Minneapolis, USA). The ANOVA test was used to determine the adequacy of the model used.D-Optimal design model with two numerical factors to point- 6, to estimate of fit 5, replicates 5 and additional center points 2 is given in Table S1.

Table S1 Experimental D-optimal design matrix generated by RSM to determine the introduction of amino groups on an adsorbent.

Run	X1, m_{DAPTES}(g)	X2 $m_{Ceel-DTPA}$(g)	Response, Content COOH (mmol g^{-1})
1	0.5	10	0.7208
2	0	2.25	0.140
3	1	10	0.705
4	1	2	0.327
5	0.28	2	0.313
6	0	10	0.766
7	1	10	0.705
8	0	4.59	0.309
9	1	2	0.327
10	0.5	6	0.492
11	1	6	0.578
12	0.5	6	0.492
13	0	2.25	0.14
14	1	10	0.705
15	0.125	7.23	0.606
16	0	10	0.766
17	0.640	2.375	0.39
18	0.56	6.57	0.506

Table S2 Box-Behnkendesign with three numerical factors and center points per block 5

Run	X1, pH	X2, $C[FeSO_4]$ (mol dm^{-3})	X3, t (min)	Response, q_e (mg g^{-1})
1	12	0.25	60	75
2	4	0.40	90	47
3	4	0.25	60	64
4	8	0.10	60	86
5	12	0.10	30	60
6	4	0.10	90	63
7	12	0.40	30	67
8	8	0.25	30	85
9	8	0.25	90	87
10	4	0.10	30	46
11	8	0.40	60	62
12	8	0.25	60	86
13	12	0.10	90	67
14	4	0.40	30	60
15	12	0.40	90	56
16	8	0.25	60	85

2.12 Measurement of membrane permeability

The water permeability of membranes was determined up to burst pressure (approx. 3.5 bar) starting from 1 bar.
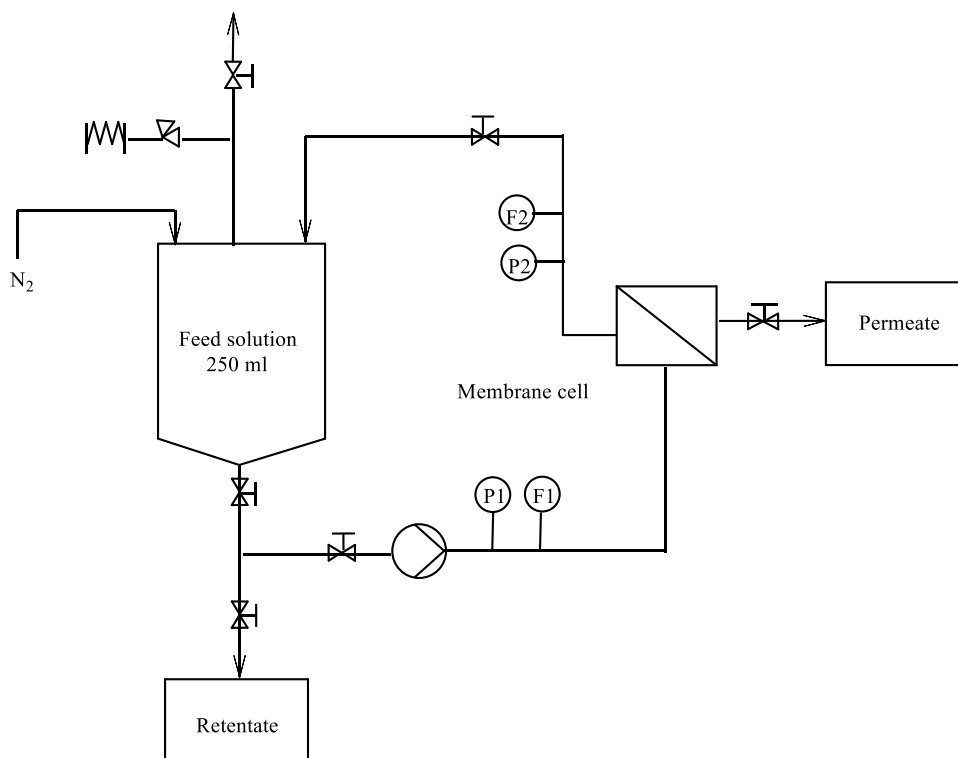
Fig. S1.Scheme of the experimental set-up for a cross-flow filtration

In the peremation test MO, MB, RB5 and DR80 dyes, and Sokalan PA30CL, 45 %, sodium-poly(acrylate), Mw 8000 g/mol (BASF) and Sokalan PA70PN, 30 %, poly(acrylic acid)/ sodium- poly(acrylate), Mw 70000 g/mol (BASF) were used.

2.13 Calculation of molecular electrostatic potential (MEP) and molecular interaction fields (MIF)

The quantitative analysis of the molecular surface was done in Multiwfn 3.7 (Griffin 1949; Lu and Chen 2012), starting from the output of B3LYP/6-31+G(d,p)//PM7 calculation (Stewart 1990, 2013; M. J. Frisch, G. W. Trucks 2016). All compounds were modeled in the ionic form. The ESP maps were rendered in VMD 1.9.3 (Humphrey et al. 1996). The percentage of polar surface, virtual log$P$ and Griffin's HLB were calculated in Vega 3.1.1 (Pedretti et al. 2004). The molecular interaction fields (MIF) (Goodford 1985)were computed in Pentacle 1.06 (Pastor et al. 2000) in order to characterize the interactions between 4 dyes (Methyl orange - MO, methylene Blue - MB, Reactive black - RB5 and Direct Red 80 - DR80) and the surface of solid phase. The sites which favourably interact with the adsorbent *via* hydrogen bonding were mapped using two MIF probes: O probe for mapping the hydrogen bond donors (HBD) of a molecule, and N1 as hydrogen bond acceptor (HBA) probe. The energy cut-off was manually set to -4 and -6 kcal/mol for O and N1 probes, respectively, as these cut-offs provided a good visualization of the differences in H-bonding characteristics between 4 dyes.

3. Results and discussion

3.1 Design of adsorption experiments using RSM methodology (Image analysis)

Image ProPlus 6.0 software was used in order to examine the porosity characteristics considering the pore size diameters and overall surface porosity. An automatic algorithm was employed in recognizing the dark (pores) and bright parts (monolith) of an image, whose red colored border was signified in Fig. S2.
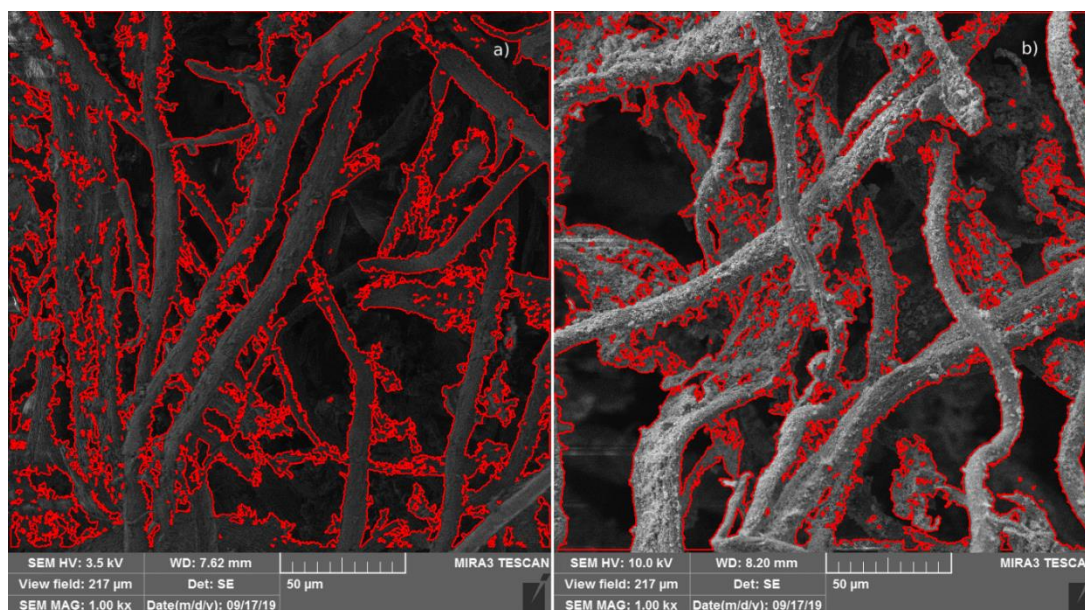

Fig. S2. SEM micrographs used for image analysis representing: (a) non-modified cellulose fibre (Cell) and (b) Cell-MG hybrid membrane

Similar pores were present for both of the materials according to the pore diameters Table S3.

Table S3 Statistical data for fibre diameter and porosity represented with mean values and standard deviation

Pore characteristics	Cell	Cell-MG hybrid membrane
Mean fibre diameter, μm	10.8±3.16	12.5±2.15
Porosity	53.75	56.50

3.2 Characterization of the adsorbent

3.2.1 Mechanical properties
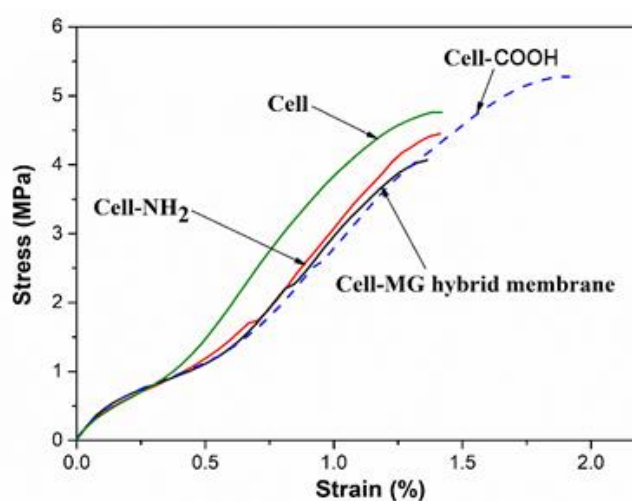
Fig. S3. Stress at break–strain curves for Cell, Cell-NH$_2$, Cell-COOH and Cell-MG hybrid membrane

According to literature, significantly higher values of tensile strength for Fe$_3$O$_4$/Regenerated Cellulose Membrane was found with a decreasing trend from 33.1 MPa at 10% of MG addition, 28.91 MPa at 20% and 4.66 MPa at 30%, as a consequence of applied modification (Kaco et al. 2017). Another example are magnetic hybrid films, derived from sisal cellulose and magnetite nanoparticles, had the value of tensile strength of 14.3 MPa (sample **FCFe$_{1.4}$**, with the magnetite mass of 4.1%) and 12.1 MPa (sample **FCFe$_{3.0}$**, with the magnetite mass of 6,8%) (Furlan et al. 2019). Magnetite-embedded cellulose fibres prepared from ionic liquid can also be found in the literature. Tensile strength of the pulp 1 sheets, obtained from International paper with a degree of polymerization, DP=487 and 10% embedded magnetite, was 159 MPa, while for pulp 2, DP=1056 and 10% embedded magnetite, gave 115 MPa(Sun et al. 2008).
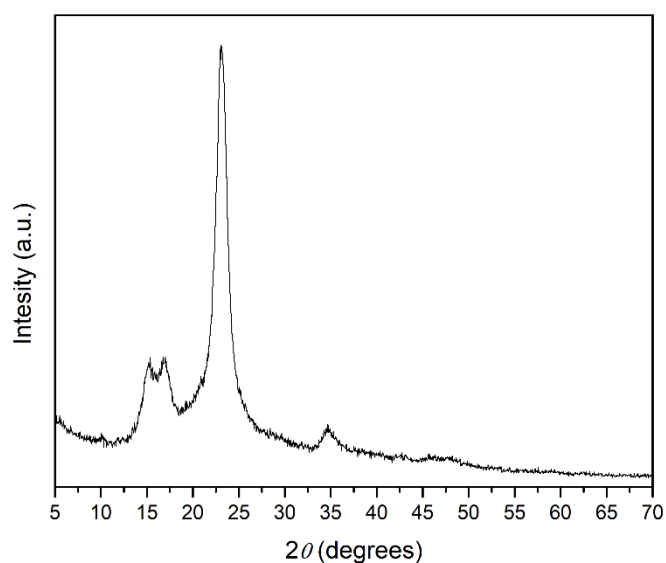
3.2.2. XRD analysis

Fig. S4. XRD pattern of cellulose

3.2.3. FTIR spectroscopy

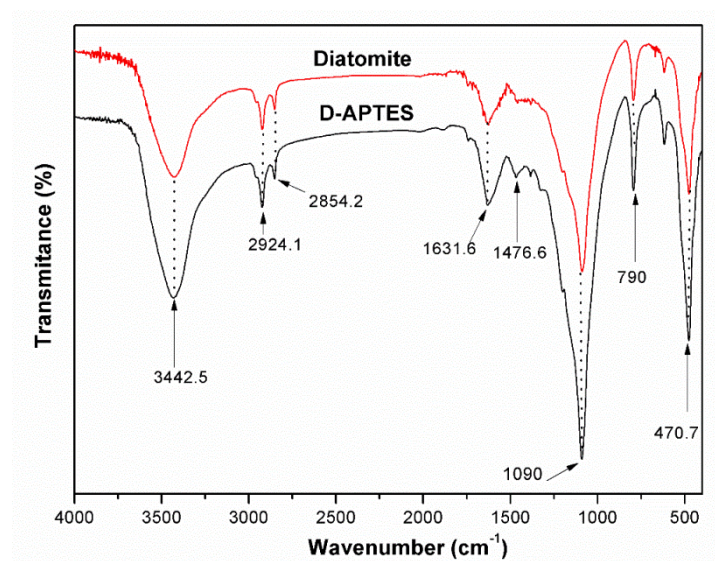Characterization of the diatomite and diatomite modified with APTES (D-APTES)

Fig. S5.FTIR spectra of diatomite and D-APTES

Diatomite silanization was evaluated by FTIR spectroscopy. The FTIR spectra of diatomite and D-APTES material in the range of 4000-500 cm^{-1}, are shown in Fig. S5. The vibrations observed at 470.7 and 1090 cm^{-1} correspond to asymmetric stretching modes of Si–O–Si bonds while the peak at 790.0 cm^{-1} corespond to the stretching vibration of Al-O-S for the diatomite and APTES modified diatomite. The deformation mode of the –NH$_3^+$group (1476.6 cm^{-1}) are observed in the spectra of D-APTES. This mode is associated with the –NH$_2$ groups from APTES. The peaks at about 3442.5 and 1631.6 cm^{-1} present the stretching

13

vibrations and the bending vibration of O–H bond of physically adsorbed water, which manifests the hydrophilic character of amorphous SiO_2. The vibrations at 2924.1 and 2854.2 cm^{-1} are related to the asymmetric and symmetric stretching modes of the C–H bond.

3.2.4 Surface Morphology analysis

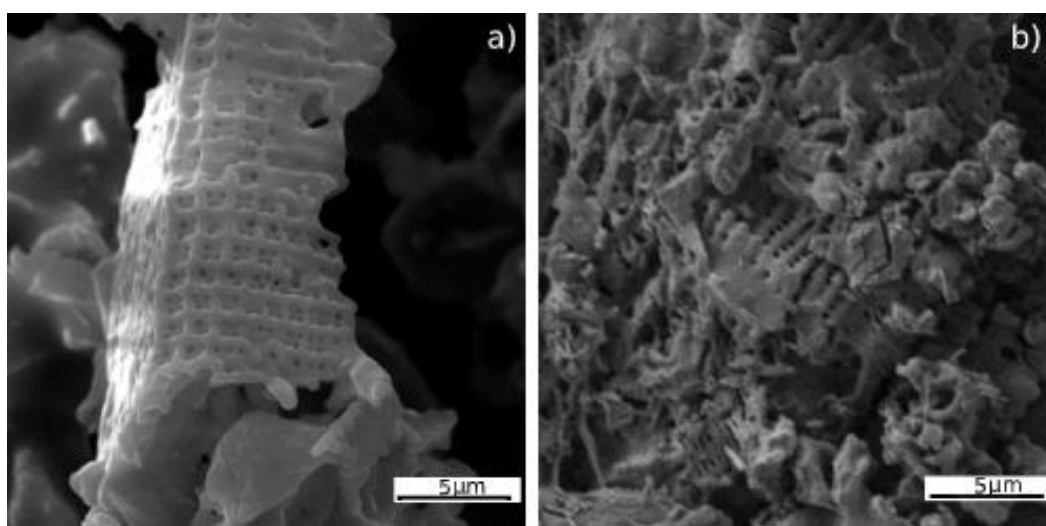Surface Morphology analysis of diatomite before and after modification

Fig. S6. SEM images of (a) diatomaceous earth and (b) D-APTES embedded into Cell-MG matrix

3.3 Adsorption study

3.3.1 Influence of solution pH on adsorption efficiency

Effectiveness of ion adsorption is associated with adsorbent surface charges and pH dependent pollutant speciation. Thus, ionic speciation of Pb^{2+}, Ni^{2+}, Cr(VI) and As(V), obtained using MINTEQ 3.0 software [https://vminteq.lwr.kth.se], are given on Fig. S7 a) – d), respectively. Fig. S7 also shows influence of the precipitation of metal hydroxide at pH>7.
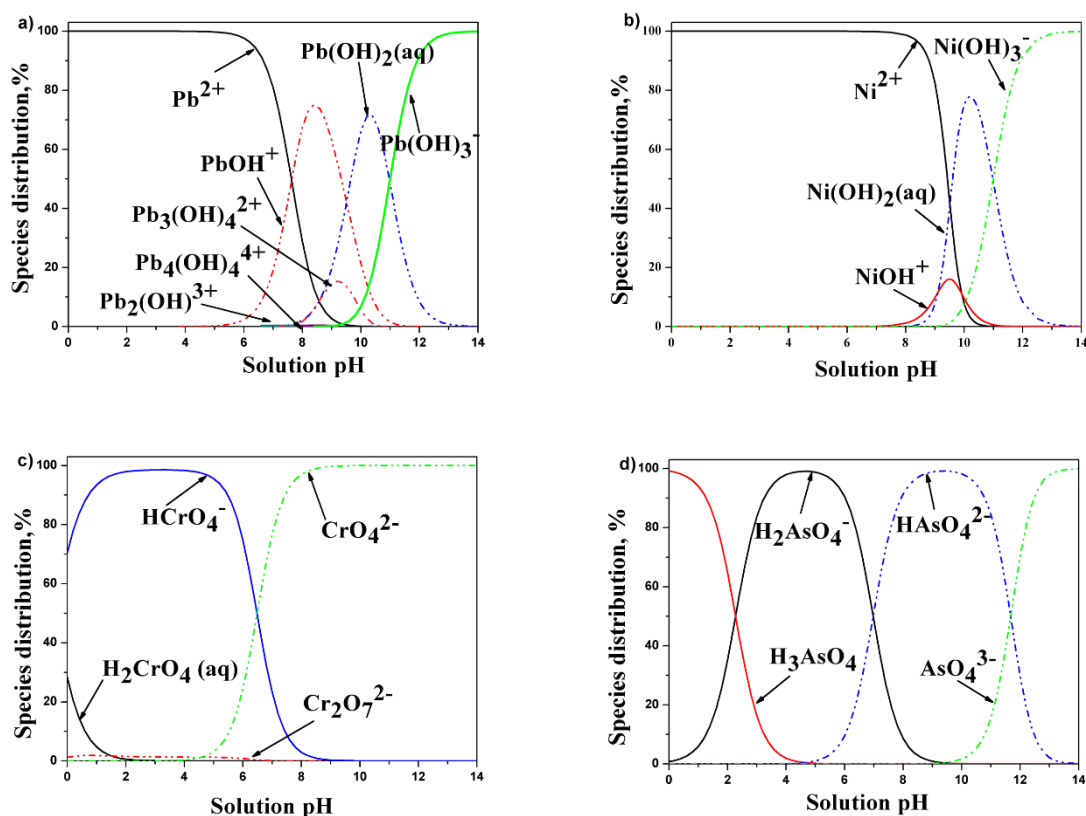
Fig. S7. Speciation of (a) Pb^{2+}, (b) Ni^{2+}, (c) Cr(VI) and (d) As(V) obtained using MINTEQ 3.0 software ($C_i = 1$ mg dm^{-3} for Pb^{2+}, Ni^{2+}, Cr(VI) and As(V), $t = 25$ °C)

Lead speciation could be present by equilibria of different forms of lead species: Pb^{2+}, $Pb(OH)^+$, $Pb(OH)_2$ and $Pb(OH)_3^-$ which are present at different pH values. Equilibrium concentrations of Pb^{2+} ionic species and precipitated $Pb(OH)_2$ was obtianed using Minteq program (Fig. S7 a)). In order to obtain reliable result overall adsorption, at pH>8, was subtracted by the value of precipitated $Pb(OH)_2$(s) (considering solubility product for $Pb(OH)_2$(s); 1.42×10^{-20}) thus giving realistic adsorption results. Analogous analysis was performed for Ni^{2+} ion (Fig. S7 b)).

The pH-dependent distribution of Cr(VI) species appears in four main forms in aqueous solution (Fig. S7. c)). The corresponding equilibrium constants (K) are: K_1=1.21, K_2=3.0x10^{-7}, K_3=35.5, K_4=0.85 (Saha et al. 2004). Dominance of the $HCrO_4^-$ atpH <6.5 and fast decreases to zero as pH increase to 8 could be obserevd. At pH > 6.5 CrO_4^{2-} dominate.

According to As(V) ionization it exist in molecular form (H_3AsO_4) at pH<2. At higher pH occurs equilibrium of arsenate anionic forms exist. From the Fig. S7 d) it can be seen that in a wide range of pH, As(V) appears in mostly as anionic species and has avalues of dissociation constants (pKa) 2.3, 7.0 and 11.5. The As(V) appears in the pH range from 2–11 as $H_2AsO_4^-$ and $HAsO_4^{2-}$ species. This condition greatly affects the adsorption process depending on adsorbent surface properteis, i.e. pH$_{PZC}$ value.

Results of pH-dependent adosprtion of Pb^{2+}, Ni^{2+} with consideration of precipitation of heavily soluble $Pb(OH)_2$ and $Ni(OH)_2$ salts, and Cr(VI) and As(V) ion are given on Figs. S8 and S9, respectively.
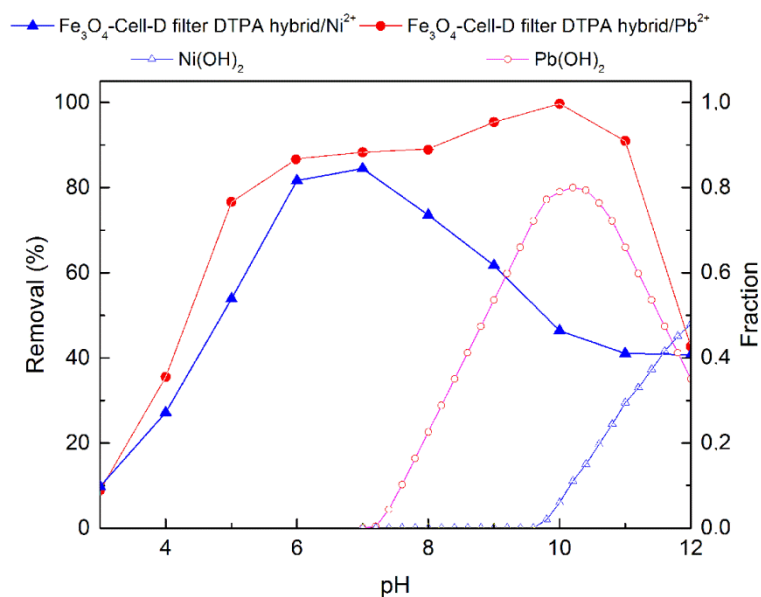
Fig. S8. The influence of pH on adsorption of Pb^{2+} and Ni^{2+} ion onto Cell-MG ($C_i[Ni^{2+}]$ = 12.50 mg dm^{-3}, $C_i[Pb^{2+}]$ = 12.10 mg dm^{-3}; m/V = 125 mg dm^{-3}, T = 298 K)

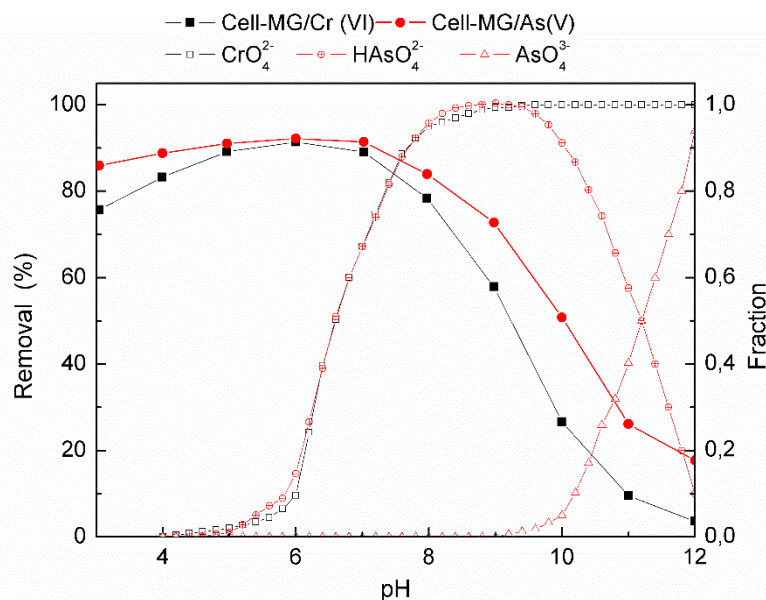
Fig.S9. The influence of pH on adsorption of Cr(VI) and As(V) ion onto Cell-MG ($C_i[Cr(VI)]$ = 13.05 mg dm^{-3}, $C_i[As(V)]$ = 7.55mg dm^{-3}; m/V = 125 mg L^{-1}, T = 298 K

Theoretical calculation and experimental study (Figs. S7 – S9) gave an overal picture on the behaviour of adsorption system. The adsorption capacity decrease at pH>7 (Fig. S8) is due to hydrolysis of metal cations and formation of ionic species with lower affinity to adsorbent surface, i.e. precipitation contribute to ion removal. Based on the results form Fig. S7 a) and b) and Fig. S8 it can be observed that precipitation of $Pb(OH)_2$ occur at pH>7 for, and Ni(OH) at pH>9.5, and according to selected optimal pH do not interfere with the result of adsorption at optimal pH. Selection of optimal pH 7 for cation is in agreement with high affinity of negatively charged surface (pH_{PZC}6.6) to positive cation. At pH higher than 8 both phenomena, precipitation and adsorption, contribute to overall adsorption (Fig S8, lines -▲- and -●-)

16

The degree of Cr(VI) and As(V) removal *vs* initial pH in presence of Cell-MG is presented in Fig. S9. Adsorption of Cr(V) and As(V) on the examined adsorbent is the best in the pH range 5-7, and gradually decrease is noticed at pH>7. At pH<pH$_{PZC}$, the negatively charged HCrO$_4^-$/CrO$_4^{2-}$ and H$_2$AsO$_4^-$/HAsO$_4^{2-}$ species (Fig. S9 c,d), take part in an electrostatic attraction with positively charged adsorbent surface, and *vice versa* at pH>pH$_{PZC}$ electrostatic repulsion is the main factor, which leads to low adsorption efficiency.

3.3.2 Adsorption isotherms

Table S4 Results for the adsorption capacities ofnon-modified diatomite, non-modified cellulose for Ni^{2+}, Pb^{2+} and Cr(VI) and As(V)

Adsorbent/ion	Adsorbent capacity (mg g^{-1})			
	Ni^{2+}	Pb^{2+}	Cr(VI)	As(V)
Diatomite(Flores-Cano et al. 2013; Du et al. 2014)	-[a]	9.91	-[a]	17.8
Diatomite[b]	12.1	11.9	12.5	-[a]
Cellulose CNFs(Voisin et al. 2017)	11.0	10.0	-	-[a]
Cellulose filter paper[b]	9.2	8.9	9.0	7.6

[a]No results reported in the literature; [b] results obtained in this study

In the present study the equilibrium adsorption data were fitted into four isotherm models: Langmuir, Freundlich, Temkin and Dubinin-Radushkevich.
In the Langmuir model Eq.S5 the adsorption is assumed to be monolayer on a homogeneous surface where all sorption sites are found to be identical and energetically equivalent. The Freundlich model Eq.S6 assumes the adsorption to be multilayer on a heterogeneous adsorbent surface with a non-uniform distribution (Veličković et al. 2012; Bozorgi et al. 2018).

$$q_e = \frac{q_m K_L C_e}{1 + K_L C_e} \text{ or linear form } \frac{C_e}{q_e} = \frac{1}{K_L q_m} + \frac{C_e}{q_m} \tag{S5}$$

$$q_e = K_F C_e^{\frac{1}{n}} \text{ or linear form } log q_e = log K_F + \frac{1}{n} log C_e \tag{S6}$$

Where C_e is metal ion concentration in solution at the equilibrium (mg dm^{-3}); q_e is the adsorption capacity at equilibrium (mg g^{-1}); q_m is the maximum adsorption capacity (mg g^{-1}) and K_L is the Langmuir equilibrium constant which is related to the affinity of binding sites (dm^3 mol^{-1});
The adsorption capacity, q_m, and affinity, K_L,calculated using Langmuir equation are the most important for analysis of adsorption process. The K_L constant, from Eq. S5, can be used to calculate a dimensionless equilibrium parameter (R_L) by the following equation:

$$R_L = \frac{1}{1 + K_L \cdot C_i} \tag{S7}$$

Where C_i is the highest initial Pb^{2+}, Ni^{2+}, Cr(VI) and As(V) concentration. The value of R$_L$ indicates the adsorption nature to be either unfavorable (R$_L$> 1), linear (R$_L$ = 1), favorable (0 < R$_L$< 1) or irreversible (R$_L$ = 0).
In Freundlich equation (Eq. S6) K_F (mg g^{-1})(dm^3 mg^{-1})$^{1/n}$ and n are the Freundlich constants and represent adsorption capacity and adsorption strength, respectively. When constant n = 1 the partition between the two phases are independent of the concentration, if value 1/n < 1 it indicates normal adsorption, while 1/n > 1 indicates cooperative adsorption.

The Dubinine-Radushkevic (D-R) isotherm model was used in order to determine if the adsorption occurred by a physical or chemical process. The linear form of this model is expressed by Eq. S8 (Mahmoud 2015):

$$\ln q_e = lnq_m - B(RT)^2 \left[ln\left(1 + \frac{1}{C_e}\right)\right]^2 \qquad \text{(S8)}$$

where B (mol^2 kJ^{-2}) and q_m (mg g^{-1}) are D-R constants, which are calculated from the slope of lnq_e versus $[RT\ln(1 + 1/Ce)]^2$ and intercept.

The Temkin isotherm model implies a uniform distribution of binding energies onto the adsorbent surface and is described by Eq. S9 (Karanac et al. 2018).

$$q_e = \frac{RT}{b} ln(AC_e) \text{ or linear form}$$

$$q_e = \frac{RT}{b} ln A + \frac{RT}{b} ln C_e \qquad \text{(S9)}$$

Where the A is the Temkin isotherm equilibrium constant (dm^3 g^{-1}) and b is Temkin isotherm constant related to the heat of adsorption.

Table S5 The results of isotherm models for Pb^{2+} and Ni^{2+} adsorption onto Cell-COOH adsorbent

Langmuir isotherm model		q_m (mg g^{-1})	K_L(dm^{3}mg^{-1})	K_L(dm^3 mol^{-1})	R^2
Ni^{2+}	25°C	35.89	3.027	177641.5	0.999
	35°C	38.27	3.146	184663.1	0.999
	45°C	40.59	3.379	198341.8	0.999
Pb^{2+}	25°C	79.48	1.025	212420.8	0.997
	35°C	82.47	1.190	246646.8	0.995
	45°C	83.28	1.399	289873.9	0.992

Table S6 The results of isotherm models for Ni^{2+} adsorption on Cell-MG

Freundlich isotherm	K_F (mg g^{-1})(dm^3 mg^{-1})$^{1/n}$	44.027	65.590	114.363
	1/n	1.294	1.303	1.309
	R^2	0.997	0.996	0.996
Temkin isotherm	A_T (dm^3 g^{-1})	3.246	4.319	6.482
	b_T	57.25	57.42	57.71
	B (J mol^{-1})	43.30	44.62	45.83
	R^2	0.869	0.862	0.854
Dubinin-Radushkevich isotherm	q_m (mg g^{-1})	76.79	84.98	98.89
	K_{ad}(mol^2 KJ^{-2})	6.64	6.54	6.39
	Ea (KJmol^{-1})	8.678	8.745	8.848
	R^2	0.918	0.9126	0.937

Table S7 The isotherm models for Pb^{2+} adsorption on Cell-MG

Freundlich isotherm	K_F (mg g^{-1})(dm^3 mg^{-1})$^{1/n}$	52.549	60.270	69.295
	$1/n$	0.739	0.735	0.743
	R^2	**0.999**	**0.998**	**0.995**
Temkin isotherm	A_T (dm^3 g^{-1})	10.057	12.085	14.146
	b_T	101.95	104.13	105.41
	B (J mol^{-1})	24.32	24.60	25.09
	R^2	0.920	0.912	0.884
Dubinin-Radushkevich isotherm	q_m (mg g^{-1})	58.96	62.05	64.56
	K_{ad}(mol^2 KJ^{-2})	8.16	8.11	8.07
	Ea (KJmol^{-1})	7.825	7.850	7.869
	R^2	0.907	0.917	0.918

Table S8 The isotherm models for Cr(VI) adsorption on Cell-MG

Freundlich isotherm	K_F (mg g^{-1})(dm^3 mg^{-1})$^{1/n}$	68.621	104.281	185.281
	$1/n$	1.330	1.327	1.308
	R^2	0.988	0.990	0.994
Temkin isotherm	A_T (dm^3 g^{-1})	4.249	5.768	9.056
	b_T	52.84	53.58	54.75
	B (J mol^{-1})	46.91	47.81	48.31
	R^2	0.822	0.828	0.843
Dubinin-Radushkevich isotherm	q_m (mg g^{-1})	85.15	96.53	116.48
	K_{ad}(mol^2 KJ^{-2})	6.41	6.29	6.10
	E_a (KJmol^{-1})	8.828	8.916	9.052
	R^2	0.896	0.915	0.942

Table S9 The isotherm models for As(V) adsorption on Cell-MG

Freundlich isotherm	K_F (mg g^{-1})(dm^3 mg^{-1})$^{1/n}$	100.11	114.67	132.27
	$1/n$	0.646	0.647	0.660
	R^2	0.984	0.987	0.972
Temkin isotherm	A_T (dm^3 g^{-1})	72.168	88.112	97.252
	b_T	171.28	175.86	174.41
	B (J mol^{-1})	14.47	14.57	15.17
	R^2	0.957	0.950	0.961
Dubinin-Radushkevich isotherm	q_m (mg g^{-1})	57.7	60.17	66.67
	K_{ad}(mol^2 KJ^{-2})	7.17	7.13	7.02
	E_a (KJmol^{-1})	8.351	8.357	8.436
	R^2	0.987	0.987	0.989

The value of R_L from Langmuir isotherm model indicates the adsorption type to be: irreversible ($R_L=0$), favourable ($0<R_L<1$), linear ($R_L=1$). Obtained R_L for the adsorption of Ni^{2+}, Pb^{2+}, Cr(VI) and As(V) on Cell-MG was in a range from: 0.130 to 0.752, 0.068 to 0.504, 0.102 to 0.717 and 0.020 to 0.127 respectively, indicating that the adsorption of these ions was favourable process.

3.3.3 Thermodynamic parameters of adsorption

Gibbs free energy ($\Delta G^{\ominus}$), enthalpy ($\Delta H^{\ominus}$) and entropy ($\Delta S^{\ominus}$) calculated from Van't Hoff equation were used for analysis of thermodynamic aspect of adsorption process Eq. S10 and S11:

$$\Delta G^{\ominus} = -RT \ln (K_L) \tag{S10}$$

$$\ln(K_L) = \frac{\Delta S^{\ominus}}{R} - \frac{\Delta H^{\ominus}}{(RT)} \tag{S11}$$

Where T is absolute temperature (K), and R is universal gas constant (J mol^{-1} K^{-1}). Langmuir adsorption constant K_L is obtained from isothermal experiments. $\Delta H^{\ominus}$ and $\Delta S^{\ominus}$ are calculated from slopes and interceptions in diagram $\ln(K_L)$ - T^{-1}, with a premise that the system attained stationary conditions.

Table S10 Ionic radius and Hydration Enthalpies for Ni^{2+}, Pb^{2+}, Cr(VI) and As(V)

Ion	Ionic radius, (Å)	Hydration Enthalpies, ΔH_h° (kJ/mol)
Ni^{2+}	0.72	-2105
Pb^{2+}	1.19	-1481
Cr(VI)	2.40	-1103
As(V)	2.48	/

3.3.4 Adsorption kinetics

Adsorption kinetics models were used to interpret the experimental data to determine the controlling mechanism of Pb^{2+}, Ni^{2+},Cr(VI) and As(V) adsorptions from aqueous solution.
Adsorption reaction models:
The pseudo-first order equation (Lagergren rate equation) is often used for the adsorption of an adsorbate from an aqueous solution. Kinetic is based on the premise that the rate of change of solute uptake with time is directly proportional to the difference in saturation concentration and the amount of solid uptake with time. The linear form pseudo-first order equationis expressed by the following Eq. S12 (Moussout et al. 2018):

$$\ln(q_e - q_t) = \ln q_e - k_1 t \tag{S12}$$

Where, q_t (mg g^{-1}) is the amount of metal ion adsorbed per unit of adsorbent, q_e (mg g^{-1}) is the adsorption capacity at equilibrium, k_1 (min^{-1}) is the pseudo-first order rate constant and t(min) is the contact time.
The linear form of pseudo-second order model (Ren et al. 2011)is given by Eq. S13:

$$\frac{t}{q_t} = \frac{1}{k_2 q_e^2} + \frac{1}{q_e} \tag{S13}$$

Where k_2 (g mg^{-1} min^{-1}) is the pseudo-second order rate constant, q_t (mg g^{-1}) and q_e (mg g^{-1}) are the adsorption capacities. The initial adsorption rate,h_2 (mg g^{-1} min^{-1}) at t→0 is defined as Eq. S14:

$$h_2 = k_2 q_e^2 \tag{S14}$$

The h_2, qe and k_2 can be obtained by the linear plot of t/q_t versus t.
One of the most useful models for describing activated chemical adsorption is the Elovich equation (Low 1960)which is given by Eq. S15:

$$\frac{1}{q_t} = \frac{1}{k_2 q_e^2} + \frac{1}{q_e} \tag{S15}$$

Where k_2 (g mg^{-1} min^{-1}) is the second-order rate constant, q_t (mg g^{-1}) and q_e (mg g^{-1}) are the adsorption capacities at any time t and at equilibrium, respectively. The initial sorption rate h_2 (mg g^{-1} min^{-1}) at t→0 is calculated as:

$$h_2 = k_2 q_e{}^2 \tag{S16}$$

In order to elucidate the possible chemisorption process for systems with the heterogeneous adsorbing surface, the following simplified form of Elovich equation was used:

$$q_t = \frac{1}{b}\ln(ab) + \frac{1}{b}\ln t \tag{S17}$$

Where q_t (mg g^{-1}) represents the adsorption capacity at any time t, a is initial ions adsorption rate (mg g^{-1} min^{-1}), while b is related to the extent of surface coverage and activation energy for chemisorption (g mg^{-1}). An approaching equilibrium factor R_E obtained from dimensionless Elovich equation is defined as:

$$R_E = \frac{1}{bq_{ref}} \tag{S18}$$

Where q_{ref} is the solid phase concentration at time t_{ref} which is the longest time in adsorption process.

The Arrhenius equationis given by Eq. S19:

$$k = Ae^{-\frac{E_a}{RT}} \tag{S19}$$

Adsorption processes are multi-step processes. A few mathematical models have been proposed to describe adsorption data, and can be classified as adsorption reaction models and adsorption diffusion models. Although both are applied as models to describe the kinetics adsorption process, they are essentially quite different. Adsorption diffusion models are based of three consecutive steps: (1) external diffusion or film diffusion (diffusion across the liquid film surrounding the adsorbent particles); (2) internal diffusion or intra-particle diffusion (diffusion in the liquid contained in the pores and/or along the pore walls); and (3) mass action (adsorption and desorption between the adsorbate and active sites).

Weber-Morris model can be used when intra particle diffusion is the only rate-limiting step, because the kinetic data can be well correlated with this model (Soldatkina and Zavrichko 2018):

$$q_t = k_i t^{\frac{1}{2}} + C_{BL} \tag{S20}$$

Where k_i (mg g^{-1} min$^{1/2}$) is intraparticle diffusion rate constant and C_{BL} is constant which reflects the boundary layer effect. In Weber-Morris model if the intraparticle diffusion is the only rate-limiting step, then the graph of q_t $vs.$ $t^{1/2}$is a streight line and pass through the origin. The values C_{BL} and k_i can be calculated from the intercept and slope of q_t vs.$t^{1/2}$ plot.

Dunwald-Wagner (D-W)(Dünwald and Wagner 1934) is a common equation used to describe intraparticle diffusion (Qiu et al. 2009). D-W relation could be expressed by Eq. S21 and S22:

$$\frac{q_t}{q_e} = 1 - \frac{6}{\pi^2} \sum_{n-1}^{\infty} \frac{1}{n^2} exp[-n^2 Kt] \tag{S21}$$

Where K (min^{-1}) is the rate constant of adsorption. Simplification of the Eq. S20 gave:

$$log\left(1 - \left(\frac{q_t}{q_e}\right)^2\right) = -\frac{K}{2.303}t \tag{S22}$$

A plot of log(1−(q/q$_t$)^2) vs t should give linear plot and the rate constant can be calculated from the slope of correlation line. D-W was rationally used to describe various types of adsorption systems and estimation of adsorption kinetics. Serin and Ellickson (Serin and Ellickson 1941)expressed the D-W equation in terms of the partial completion of the reaction Eq. S23

$$k_{DW}t = \frac{\pi^2}{r^2}Dt = ln\frac{6}{\pi^2(1-\alpha)} = -log\left(1 - \left(\frac{q_t}{q_e}\right)^2\right) \tag{S23}$$

Where D is the diffusion coefficient of the migrating species and k_{DW} is the Dunwald-Wagner isothermal reaction constant, r is the initial radius of the reacting particle, α is the fractional

completion of reactions at time t, q_e and q_t are the adsorption capacity of adsorbent (mg g^{-1}) at equilibrium and appropriate t, respectively.

Homogeneous solid diffusion model (HSDM) is a typical intra-particle diffusion model which can describe mass transfer in an amorphous and homogeneous sphere (Viegas et al. 2014). HSDM model can be expressed by differential equation:

$$\frac{\partial q}{\partial t} = \frac{D_s}{r^2}\frac{\partial}{\partial r} = \left(r^2 \frac{\partial q}{\partial r} \right) \tag{S24}$$

Where Ds is intraparticle diffusion coefficient, r radial position, and q the time-dependent adsorption capacity. The precisely solution to Eq.S26 for the defined adsorption condition was given by Crank :

$$\frac{q_t}{q_e} = 1 + \frac{2R}{\pi r}\sum_{n-1}^{\infty}\frac{(-1)^n}{n}\sin\frac{n\pi r}{R}exp\left[\frac{-D_S t\pi^2 n^2}{R^2}\right] \tag{S25}$$

The equation discussed above is generally somewhat valid in a short time.

The value of Ds for long-time data can be also determined by plotting of ln(1- q_t/ q_e) vs t.

$$ln\left(1 - \frac{q_t}{q_e}\right) = \frac{-D_S\pi^2}{R^2}t + ln\frac{3}{\pi^2} \tag{S26}$$

The Eq. S26 refers to the change rate of surface concentration q_t with time t at any distance R from the center of adsorbent particle during adsorption for a constant boundary condition and developed a nonlinear equation for the total mass of adsorbate present on the surface of a unit weight of adsorbent q_t for a particular contact time t. In case there is none film diffusion limitation, this equation can be generalized into a non-dimensional. The homogeneous solid diffusion model equations are solved numerically, for a single solute with uniform adsorbent size.

Table S11 Pseudo-first, pseudo-second and second order reaction kinetic parameters for the adsorption of Pb^{2+}, Ni^{2+}, Cr(VI) and As(V) ions by Cell-MG adsorbent

Ion/order of kinetic law		Pseudo-first	Pseudo-second	Second order
Pb^{2+}	q_e	45.384	89.183	89.183
	k (k_1, k_2)	0.0266	0.0026	0.0058
	R^2	0.942	0.993	0.995
Ni^{2+}	q_e	25.952	83.435	83.435
	k (k_1, k_2)	0.0228	0.0065	0.0036
	R^2	0.084	0.999	0.919
Cr(VI)	q_e	13.060	97.261	97.261
	k (k_1, k_2)	0.0046	0.0031	0.0083
	R^2	0.265	0.994	0.934
As(V)	q_e	26.614	58.952	58.952
	k (k_1, k_2)	0.0335	0.0023	0.0109
	R^2	0.942	0.998	0.840

3.3.5 Desorption

In this research, the obtained Cell-MG hybrid membrane was tested in the optimization of desorption study by changing the concentration and type of regenerating agent. In ion removal processes from aqueous solutions, desorption and depletion of adsorbents are essential factors as they control the economy of water treatment technology and thus it is very important to achieve high-efficiency adsorbents as well as to develop optimal desorption technology. Cation desorption increases with pH increase, whereby the use of sodium hydrogen carbonate and sodium hydroxide can be provided >90% bonded cation release. Desorption of ions in acidic media also provide a high desorption efficiency by applying an

acid regenerating agent such as HCl, H_2SO_4, HCOOH and CH_3COOH. The acidic regenerating agent has the ability to donate protons while causing simultaneous protonation of the amino group. To restore the adsorption potential of the Cell-MG membrane after desorption, it is necessary to activate the adsorbent using a basic solution. For this study, it was found that the efficient desorption system contained alkali hydrogen carbonate ($NaHCO_3$, 4%) and salt (NaCl, 2%). The reusability results for the Cell-MG hybrid membrane, after three adsorption-desorption cycles for Ni^{2+}, Pb^{2+}, $CrO_4^{2-}/HCrO_4^-$ and $HAsO_4^{2-}/H_2AsO_4^-$ ions, showed low reduction in adsorption efficiency for 18 %, 22 %, 19 % and 25 %, respectively. The conducted study clearly showed that the adsorbent produced by the methods outlined in this paper is very effective in removing ions from aqueous solutions, and can be used in three adsorption-desorption cycles, therefore it is also a very useful technology for water treatment.

3.3.6. Monolayer model for single-compound adsorption and adsorption mechanism

$$\varepsilon = k_B T ln\left(\frac{c_s}{c_{1/2}}\right) \tag{S27}$$

where k_B Boltzmann constant, c_s is the solubility of the heavy metal and $c_{1/2}$ is the concentration at half saturation (Sellaoui et al. 2016a, b).

$$Z_{gc} = 1 + e^{\beta(\varepsilon+\mu)} \tag{S28}$$

$$Z_{gc} = e^{\beta(\varepsilon+\mu)N_M} \tag{S29}$$

$$Q = \frac{nN_M}{1+\left(\frac{c_{1/2}}{c}\right)^n} \tag{S30}$$

In these expressions, ε represents the adsorption energy of the receptor site, μ is the chemical potential of the adsorbed state determined from the Gibbs free energy, β is the Boltzmann factor, defined as $1/(k_B T)$, Q is the adsorption capacity, n is the number of ions per site, N_M is the density of receptor site, and c is the heavy metal ion/oxyanion equilibrium concentration (Sellaoui et al. 2016a, b).

Adsorption mechanism of Pb^{2+} and Ni^{2+} cation, and $H_2AsO_4^-/HAsO_4^{2-}$ and $HCrO_4^-/CrO_4^{2-}$

oxyanions ions removal by the Cell-MG

Majority of adsorption performances of a magnetite based adsorbent could be explained by existence of pH-dependent surface functionalities: OH_2^+, OH, and O^- groups. At pH<7, OH_2^+ and OH forms of magnetite surface functionalities dominate, and resent groups with participate in binding of molecular and ionic forms of oxyanions and cations (Rusmirovic et al. 2019). The adsorption mechanism onto Cell-MG consist from proton exchange from surface hydroxyl groups with cation. Magnetite surface, populated with amphoteric hydroxide functional group (Sherman and Randall 2003), which also could act as proton-accepting and proton-donating sites. Due to such properties surface hydroxyl groups could react with electron-deficient cation by forming either surface complexes or ion pair assembly due to electrostatic interactions, depicted as shown by Eqs. (S31) and (S32) (Drah et al. 2017):

$$FeOH + M^{2+} \rightarrow (FeO^-)M^+ + H^+ \tag{S31}$$

$$2FeOH + M^{2+} \rightarrow (FeO^-)_2M + 2H^+ \tag{S32}$$

In the course of adsorption, described by Eqs. (S31) and (S32), two processes dominate: release of H^+ and creation of a coordinative complex of cation with hydroxy groups. Coordination complexes created by hydrated cationi is a mainly situated in the outer plane of charge distribution profile by forming "outer sphere" complexes. The complexation of

partially dehydrated cation, tightly bonded to surface hydroxyl group, create the "inner sphere" complexes. Analogous adsorption mechnaism was found for oxyanions onto magnetite (Sherman and Randall 2003; Taleb et al. 2016). Using EXAFS method, based on oxyanion-Fe distance, Fendorf*et al*. (Manning et al. 1998) defined existence of three different arsenate surface complexes on goethite: a monodentate, a bidentate-binuclear and a bidentate-mononuclear where the prevalent of complex depends on coverage degree.

Mechanism of ions adsorption on magnetite was studied using FTIR spectroscopy, and corresponding FTIR spectra obtained after As(V) and Pb^{2+} adsorption onto Cell-MG are given on Fig. S10.
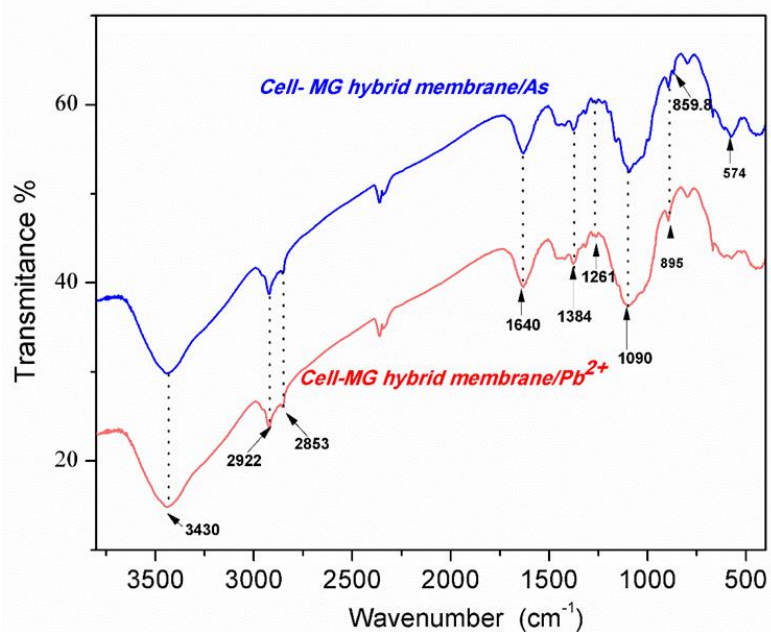
Fig. S10. FTIR spectra of Cell-MG hybrid adsorbent after As(V) and Pb^{2+} adsorption

Observed differences in the spectras before and after As(V) adsorption can be summarized: appearance of a low intensity peak at 860 cm^{-1} in the Cell-MG hybrid/As(V) spectrum is assigned to coordinated arsenic species, i.e. As-O stretching vibration. The As–O–Fe bond strength increases with increasing of the coordination number, what indicate that uncomplexed/unprotonated As–O–Fe was located at a higher frequency (895 cm^{-1}), while the one of the complexed As–O–Fe band was located at a lower frequency (860 cm^{-1}). The intensive band at 574 cm^{-1}, assigned to Fe-OH vibrations present at magnetite surface is weakened after arsenate adsorption. This region corresponds to vibration of As-O-Fe complexed arsenate species. After adsorption of Pb^{2+} the intensity of the peak at 574 cm^{-1}significanlty decrease.

3.4 Application of Cell-MG hybrid adsorbent for mining wastewater treatment

Nowadays, there is a strong need for adsorbent materials that have the capacity for removing simultaneously both anions and cations from mining solutions. Evaluation of Cell-MG hybrid adsorbent for cation and anion removal from real water samples was performed using wastewater from the mining industry (located in Serbia).

Table S12 The removal of anions/cations by Cell-MG from real water sample

Ions	Wastewater before treatment mg dm^{-3}	Wastewater after treatment mg dm^{-3}	Removal %
Pb^{2+}	3.2	1.7	46.8
Cu^{2+}	120.4	89.6	25.6
Ca^{2+}	320.3	38.4	23.20
Mn^{2+}	15.1	11.7	22.5
Cd^{2+}	5.2	3.2	38.5
Ni^{2+}	20.4	11.0	46.1
Zn^{2+}	25.3	19.9	21.3
Cr(VI)	0.04	0	100.00
As(V)	16.3	8.6	47.2
SO$_4^{2-}$	4687.0	4049.6	13.6
Cl$^-$	116.7	114.1	2.2

(pH adjusted to ~ 6.5)

Obtained results, presented in Table S12, showed increased adsorption of Cell-MG hybrid adsorbent for certain ion. In general, adsorption efficiency of anions/cations removal depends not only on the pollutant nature, physico-chemical properties of the solution such as pH, temperature, surface properties of the adsorbent and the properties of other species which may interfere with the pollutant lowering adsorption performance (ionic radius, electronegativity, etc.). In this study effect of interfering anions showed significant influence on decrease of the efficiency of all present ions removal. Competitive adsorption in multi-component system, due to different affinity of present ions to adsorbent surface, Ni^{2+}, Pb^{2+}, Cr(VI) and As(V) for adsorption sites.

3.5 Membrane performance with respect to dyes removal

3.5.1 Permeation properties

The membrane permeation flux is defined as the volume flowing through the membrane per unit area per unit time (Eq. (S33)):

$$J = \frac{V}{At} \tag{S33}$$

where V is the volume of the permeate (dm^3), A is the effective membrane area (m^2) and t is the time (h). The water treatment performance test was carried on the obtained membranes. The rejection was calculated by the following equation:

$$Rejection\ (\%) = \left(1 - \frac{Cp}{Cf}\right) x100\ \% \tag{S34}$$

The dye permeate flux, defined by Eq. (S33), was applied to study the permeation properties of Cell-COOH and Cell-MG membrane, whereas the rejection ratio (R) was calculated by Eq. (S34). Aqueous MO, MB, RB5, DR80 and three range of the molecular weight of sodium alginate (10-200 ppm) was used in a permeation experiments. The estimated average pore size of the support indicate micro-filterability of Cell-MG and possibility to achieve high flux. It is in agreement with high memebrane porosity: 65% for Cell-COOH and 58% for Cell-MG (Table 1). Highly porous membrane provide condition for high loading flux with adsorbate of wide range of properties, considering geometrical feature of adsorbate and modified fibres surface properties. The water permeability, i.e. water flux, of the Cell-COOH

and Cell-MG membranes was evaluated in cross-flow system (Fig.S1) at the variable rate condition (applied pressure). The obtained results are given in Fig. S11.
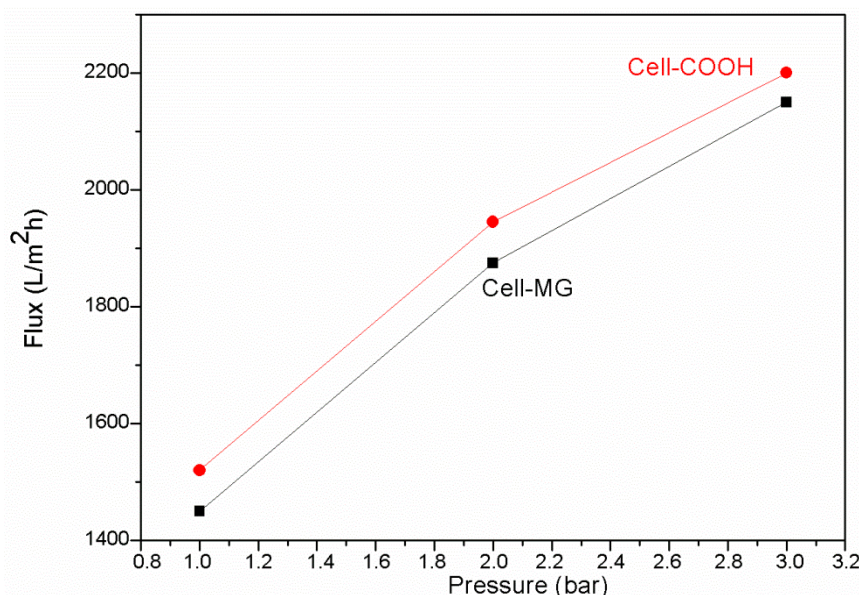

Fig. S11. Water flux versus pressure for Cell-COOH and Cell-MG

From the Fig.S11 it can be seen that flux was significant, and it increase to 3 bar pressure until membrane rupture. Similar material density and porosity provide condition for similar hydrodynamic behavior of both adsorbents (Fig. S11). The water permeability was 1433 L m^{-2} h^{-1} bar^{-1} for the Cell-MG, while increased value was found for Cell-COOH of 1560 L m^{-2} h^{-1} bar^{-1}.

Effects of different dyes concentration

The change of rejection and flux was studied using feed solutions which contained MO, MB, RB5, DR80 and sodium alginate concentration between 10 and 80 mg dm^{-3} RB5 and DR80 rejection was lower than 10 % at dye concentration of 40 mg dm^{-3} and after it increases slowly with concentration increase. Rejection was 14 % when the dye concentration increase to 80 mg dm^{-3}. Otherwise, good rejection was obtained with sodium alginate as a results of repulsion force, i.e. negative charges repulsion, along with polymer aggregation (at pH 7). Flux increases with sodium alginate concentration increase and reach constant value at > 80 mg dm^{-3}.Two phenomena contribute to such sieving behaviour: sodium alginate accumulation on the membrane surface with increasing concentration, i.e. deposit building on the membrane/solution interface, and adsorption. At the point of maximum adsortion the formed sodium alginate deposit did not contribute to increase of flux resistance membrane resistance due to membrane porosity. In general such behaviour of Cell-MG indicates that couple effect play a significant role: steric effects (size of molecule), charge interaction and adsorption affinity.

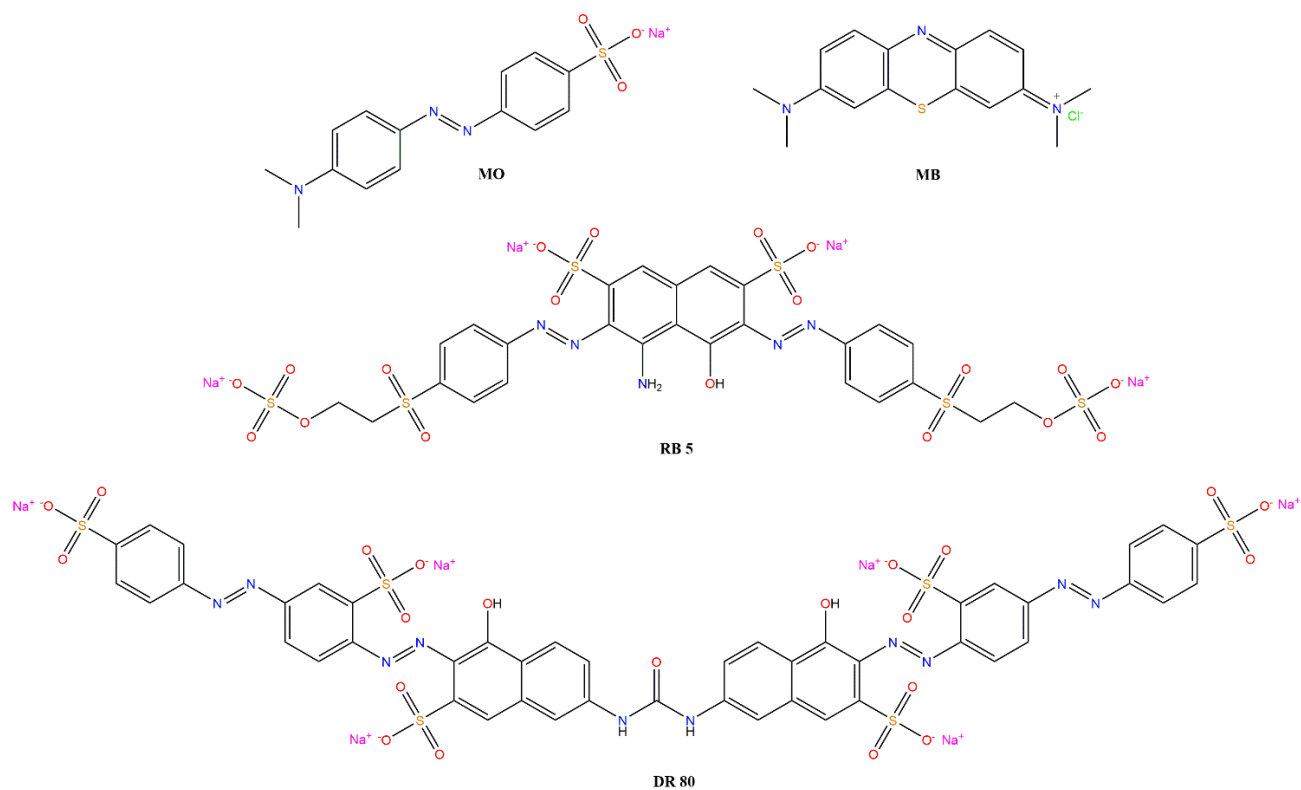## 3.5.2. Adsorption removal of dyes

Fig. S12. Structure of the dyes used in adsorption experiments

Table S13 PSO kinetic parameters for the adsorption of dyes by Cell-MG hybrid membrane

Dye/order of kinetic law		Pseudo-second
Methyl orange	q_e	68.462
	$k\ (k_1, k_2)$	0.0014
	R^2	0.999
Methylene blue	q_e	70.929
	$k\ (k_1, k_2)$	0.0008
	R^2	0.978
Reactive black 5	q_e	103.683
	$k\ (k_1, k_2)$	0.00025
	R^2	0.960
Direct red 80	q_e	143.33
	$k\ (k_1, k_2)$	0.00015
	R^2	0.991

Table S14 Calculated dimensions of dyes (x, y, z – coordinate system, measured value given in Angstroms)

dye	length, x	width, y	height, z
MO	17.4422	7.1991	5.5419
MB	16.6448	7.9283	4.1855
RB5	31.6603	12.7094	8.6634
DR 80	42.8540	15.8783	10.8547

Table S15 Several geometric and hydrophilicity/lipophilicity parameters of 4 dyes

	Volume, ($Å^3$)	Surf. area, ($Å^2$)	% PSA	% APSA	Virtual log$P$	Griffin's HLB (Griffin 1949)
MO	366.63	337.20	27.78	72.22	3.25	5.34
MB	353.45	320.12	12.06	87.94	5.45	2.53
RB5	889.23	761.19	56.24	43.76	-1.36	11.06
DR80	1221.23	1045.40	49.18	50.82	-0.81	9.74

PSA and APSA – polar and apolar surface area
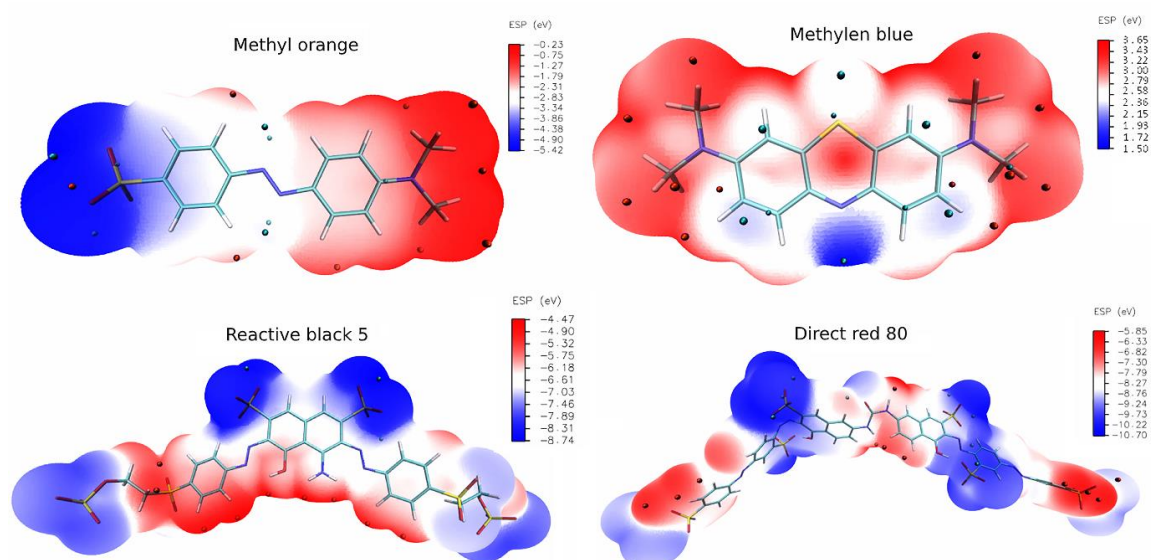
Fig. S13. ESP maps with the distribution of negative (cyan blue spheres) and positive (orange spheres) electronic density

3.6 Bed column study

The operational values (flow rate and concentration of pollutants in the medium) of the selected variables are shown in Table S16.

Table S16. Experimental plan, D-optimal desing, Design Model Quadratic, model point - 9, to estimate lack of fit - 5, replicates - 5.

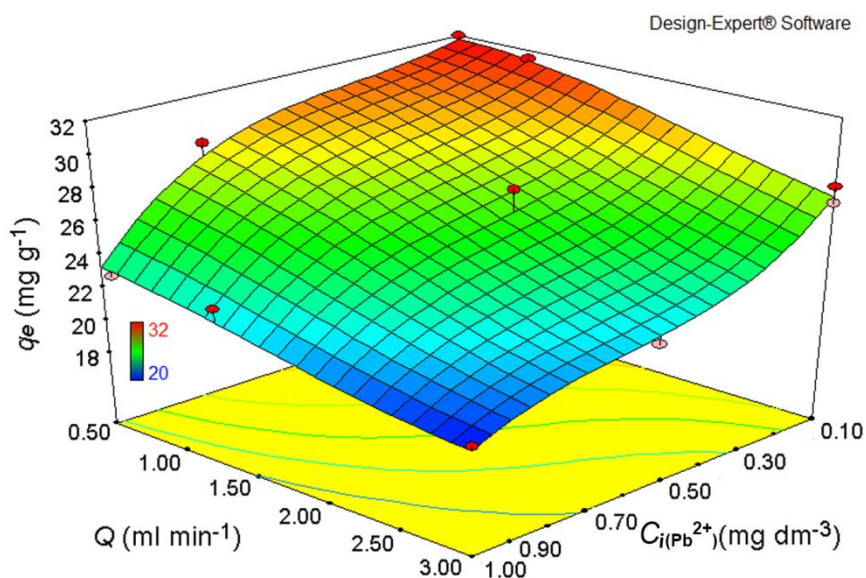| Run	C_i (mg dm^{-3})	Q (cm^3 min^{-1})	T(°C) Level 1 – 45 °C Level 2 – 25 °C	Response q_e, (mg g^{-1})
1	3.00	5.00	Level 2	56.21
2	2.45	2.75	Level 2	48
3	0.77	5.00	Level 1	63
4	3.00	0.50	Level 1	40
5	1.23	2.86	Level 1	60
6	0.50	2.75	Level 2	59
7	0.50	5.00	Level 2	64
8	0.50	5.00	Level 2	64
9	0.50	0.50	Level 1	46
10	1.75	0.50	Level 1	42
11	1.38	1.28	Level 2	48
12	3.00	5.00	Level 1	55.1
13	3.00	2.90	Level 1	44.1
14	1.89	4.86	Level 1	56
15	3.00	0.50	Level 2 C	41.1
16	3.00	0.50	Level 2	41.1
17	3.00	5.00	Level 2	56.21
18	0.50	0.50	Level 1	46
19	3.00	5.00	Level 1	55.1

Fig. S14. Contour diagrams represent relation between concentration of pollutant and flow rate of influent water versus capacity q_e (m$_{ads}$ =430 mg; pH= 7)

The Yoon–Nelson model is based on the hypothesis that the rate of decrease in the probability of adsorption for each adsorbate molecule is proportional to the probability of adsorbate adsorption and the probability of an adsorbate's breakthrough point. This model

does not require detailed information about the type of adsorbent, the characteristics of adsorbate and the physical properties of the adsorption bed (Biswas and Mishra 2015). The Yoon–Nelson equation in linearized form is expressed as Eq. S35:

$$\ln\left(\frac{C_t}{C_0-C_t}\right)= K_{YN}\Theta - K_{YN}t \tag{S35}$$

where C_0 (mol dm^{-3}) is initial concentration of heavy metal, C_t (mol dm^{-3}) is concentration of heavy metal at time t, t (min) is flow time, Θ(min) is time required for 50 % breakthrough, K_{YN}(min^{-1}) is the Yoon-Nelson rate constant.

The Bohart-Adams model is based on the assumption that the rate of adsorption is proportional to the residual concentration of the adsorbent and concentration of adsorbing species (Biswas and Mishra 2015). Linear form of Adams- Bohart model is given by the equation below: Eq. S36:

$$\ln\left(\frac{C_t}{C_0}\right) = K_{AB}C_0t - \frac{K_{AB}N_0Z}{U_0} \tag{S36}$$

Where, C_i (mol dm^{-3}) is initial concentration, C_t (mol dm^{-3}) is concentration of effluent at time t, Z (cm) is bed depth of column, N_0 (mg dm^{-3}) is maximum dye uptake capacity per unit volume of adsorbent column, U_0 (cm min^{-1}) is linear velocity of influent dye solution, K_{AB} (dm^3 mg^{-1} min^{-1}) is the kinetic constant. Modified dose-response model (Lee et al. 2015), Eq. S37:

$$\frac{C}{C_0} = 1 - \frac{1}{1+(\frac{Qt}{b})a}, q_0 = \frac{bc_0}{m} \tag{S37}$$

Where, q_0 (mg g^{-1}) is the equilibrium uptake per g of the adsorbent, m (g) is the amount of the adsorbent in the column, parameters a and b are from the modified dose-response model.
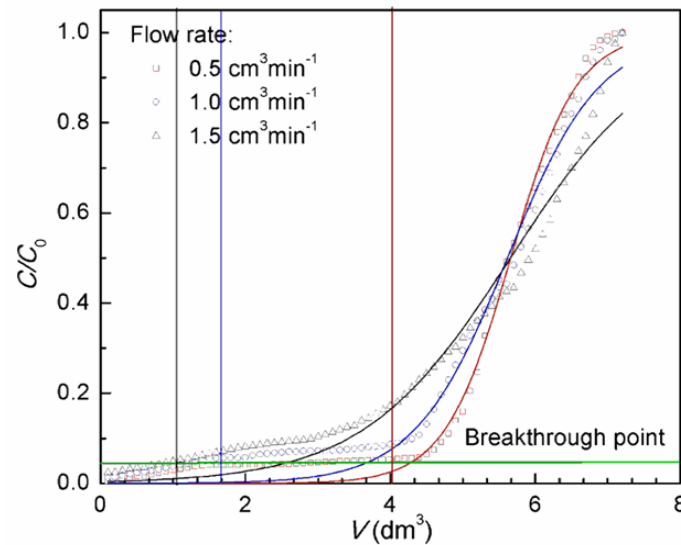

Fig. S15. The Bohart-Adams fitted breakthrough curves of Ni^{2+} adsorption by Cell-MG at different flow rate (C_i[Ni^{2+}]= 6.10 mg dm^{-3}; m_{ads} =430 mg; t=25 °C; pH= 7, BV= 0.8 cm^{-3})
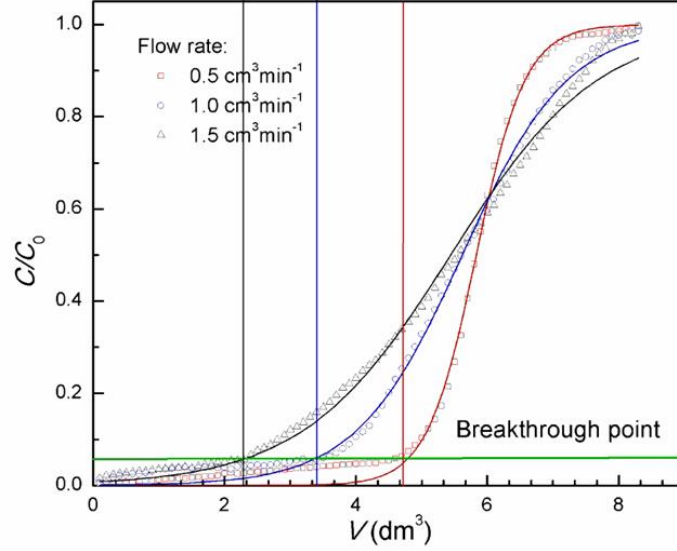
Fig. S16. The Bohart-Adams fitted breakthrough curves of Pb^{2+} adsorption by Cell-MG at different flow rate ($C_i[Pb^{2+}]= 6.20$ mg dm^{-3}; $m_{ads} = 430$ mg; $t=25$ °C; pH=7, BV=0.8 cm^3)
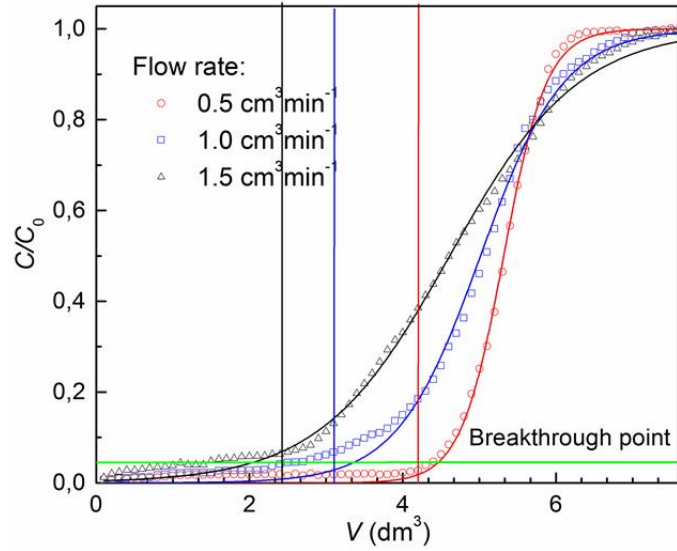

Fig. S17. The Bohart-Adams fitted breakthrough curves of Cr(VI) adsorption by Cell-MG at different flow rate ($Ci[Cr(VI)] =6.20$ mg dm^{-3}; $m_{ads} = 430$ mg; $t = 25$ °C; pH = 6, BV = 0.8 cm^3)

Clark model (Lee et al. 2015), is given by Eqs. S38-S41. Clark model was based on the use of a mass-transfer concept in combination with the Freundlich isotherm constant.

$$\frac{C}{C_0} = \left(\frac{1}{1+Ae^{-rt}}\right)^{\frac{1}{n}-1} \tag{S38}$$

$$A = \left(\frac{C_0^{n-1}}{C_b^{n-1}} - 1\right) e^{rt_b} \tag{S39}$$

$$r = \frac{k_T}{U_0} \upsilon(n-1) \tag{S40}$$

Where n is the Freundlich constant, C_b is the concentration at breakthrough (mmol·L^{-1}), k_T is the mass-transfer rate coefficient (min^{-1}) and υ is the migration velocity of the concentration fronts in the bed (cm·min^{-1}), determined by the following equation: Eq. S41

$$\upsilon = \frac{U_0 C_0}{N_0 + C_0} \tag{S41}$$

31
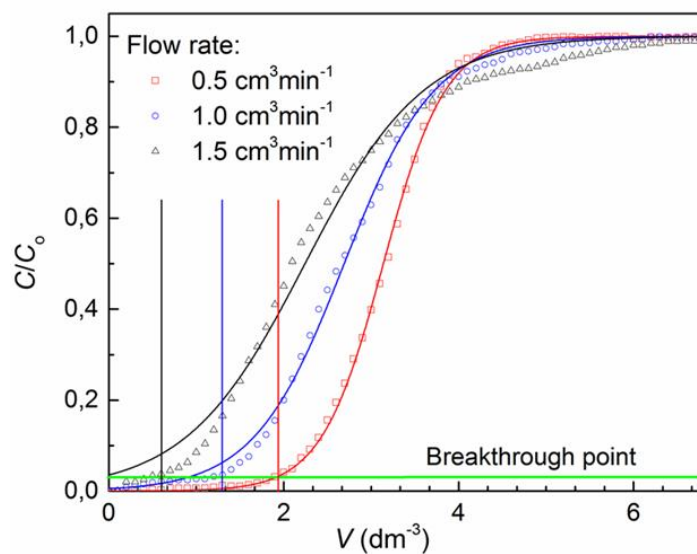
Fig. S18.The Bohart-Adams fitted breakthrough curves of As(V) adsorption by Cell-MG at different flow rate (C_i[As(V)]= 5.00 mg dm^{-3}; m_{ads} = 430 mg; t = 25 °C; pH = 6, BV = 0.8 cm^3)

Table S17 Results of non-linear fitting of experimental data obtained using Clark adsorption model and ODR iteration algorithm

Clark	F ml min^{-1}	A	r (min^{-1})	R^2
Cr (VI)		664.3	0.372	0.989
Pb^{2+}	0.5	762.7	2.167	0.995
Ni^{2+}		535.1	1.472	0.983
As (V)		189.8	2.027	0.999
Cr (VI)		178.4	0.245	0.970
Pb^{2+}	1	64.32	0.991	0.993
Ni^{2+}		39.74	1.016	0.959
As (V)		21.86	1.377	0.999
Cr(VI)		28.85	0.183	0.995
Pb^{2+}	1.5	10.44	0.688	0.985
Ni^{2+}		3.42	0.568	0.914
As (V)		7.449	1.052	0.999

3.7 Overview of adsorption capacities and kinetic data of cellulose based adsorbents

Table S18 Examples of maximum adsorption capacities (q_{max}) of cellulose-based adsorbents reported (mg g^{-1})

Refer.	Adsorbent	Initial concentration (mg dm^{-3})	T (^{0}C)	Pb^{2+}	Ni^{2+}	Cr(VI)	As(V)	Adsorption isotherms, kinetics
(Najib and Christodoulatos 2019)	Cellulose nanofibrils (CNF)	10	25				25.5	Langmuir; pseudo-second-order, k_2 = 0.1239 g mg^{-1} min^{-1}
(Kumar and Sharma 2019)	Grafted copolymer of cellulose	100	30	98.0	74.5			Langmuir; PSO; intra particle diffusion mechanism; k_2 = 6.83×10^{-3} g mg^{-1} min^{-1} (for Pb^{2+}) k_2 = 9.64×10^{-3} g mg^{-1} min^{-1} (for Ni^{2+})
(Olguín et al. 2013)	Peanut husk	25	-			33.1		Langmuir;
(Sun et al. 2014)	Magnetic cellulose nanocomposite		25			171.5		Langmuir; pseudo-second-order;
(Yu et al. 2013)	Cellulose nanocrystals	300	25±2	43.1				Langmuir; pseudo-second-order, k_2 = 1.62×10^{-2} g mg^{-1} min^{-1}
(Kardam et al. 2014)	Non-modified Cellulose (CNF-OH) mechanical treated	25	rt		11.2			Langmuir;

Table S18. Continue

(Kardam et al. 2014)	Non-modified cellulose (CNF-OH) mechanical treated	25	rt	10.2			Langmuir
(Aquino et al. 2018)	Cellulose acetate/polycaprolactone reinforced nanostructured membrane	100	-	70.5			Freundlich; pseudo-second-order
(Sharma et al. 2016)	Cellulosic-ferric oxide system	10	rt			5.45	Langmuir ; pseudo-first-order
(Tabatabaeefar et al. 2019)	PSM/EC cellulose microfiber	250	45	44.6			Liu; Double-exponential model;
(Vadakkekara et al. 2019)	Macro sodium cellulose maleate	300	40	20			Freundlich; intra particle diffusion model and PSO;
(Vadakkekara et al. 2019)	Micro sodium cellulose maleate	300	40	40			Freundlich; pseudo-second-order;
(Davarnejad et al. 2018)	Regenerated cellulose	32.5	25		91%		-
(Kundu et al. 2019)	β-Cyclodextrin-Cellulose/Hemicellulose-Based Hydrogels	500	25		18.44		Langmuir; pseudo-second-order, $k_2 = 2.63 \times 10^{-3}$ g mg^{-1} min^{-1}
(Awang et al. 2019)	Regenerated cellulose membrane	100	-			18.13	Langmuir; pseudo-first-order;
(Pakade et al. 2017)	Macadamia nutshell powder	100	-			42.44	Langmuir; pseudo-second-order $k_2 = 7.22 \times 10^{-3}$ g mg^{-1} min^{-1}

5. References

Aquino RR, Tolentino MS, Elacion RMPD, et al (2018) Adsorptive removal of lead (Pb^{2+}) ion from water using cellulose acetate/polycaprolactone reinforced nanostructured membrane. IOP Conf Ser Earth Environ Sci 191:2–10. https://doi.org/10.1088/1755-1315/191/1/012139

Awang NA, Wan Salleh WN, Ismail AF, et al (2019) Adsorption behavior of chromium(VI) onto regenerated cellulose membrane. Ind Eng Chem Res 58:720–728. https://doi.org/10.1021/acs.iecr.8b02366

Biswas S, Mishra U (2015) Continuous fixed-bed column study and adsorption modeling: Removal of lead ion from aqueous solution by charcoal originated from chemical carbonization of rubber wood Sawdust. J Chem 2015:. https://doi.org/10.1155/2015/907379

Bozorgi M, Abbasizadeh S, Samani F, Mousavi SE (2018) Performance of synthesized cast and electrospun PVA/chitosan/ZnO-NH2 nano-adsorbents in single and simultaneous adsorption of cadmium and nickel ions from wastewater. Environ Sci Pollut Res 25:17457–17472. https://doi.org/10.1007/s11356-018-1936-z

D'Halluin M, Rull-Barrull J, Bretel G, et al (2017) Chemically modified cellulose filter paper for heavy metal remediation in water. ACS Sustain Chem Eng 5:1965–1973. https://doi.org/10.1021/acssuschemeng.6b02768

Davarnejad R, Moraveji MK, Havaie M (2018) Integral technique for evaluation and optimization of Ni(II) ions adsorption onto regenerated cellulose using response surface methodology. Arab J Chem 11:370–379. https://doi.org/10.1016/j.arabjc.2015.05.022

Drah A, Tomić NZ, Veličić Z, et al (2017) Highly ordered macroporous γ-alumina prepared by a modified sol-gel method with a PMMA microsphere template for enhanced Pb^{2+}, N^{i2+} and Cd^{2+} removal. Ceram Int 43:13817–13827. https://doi.org/10.1016/j.ceramint.2017.07.102

Du Y, Zheng G, Wang J, et al (2014) MnO2 nanowires in situ grown on diatomite: Highly efficient absorbents for the removal of Cr(VI) and As(V). Microporous Mesoporous Mater 200:27–34. https://doi.org/10.1016/j.micromeso.2014.07.043

Dünwald H, Wagner C (1934) Methodik der Messung von Diffusiongeschwindigkeiten bei Losungsvorgangen von Gasen in festen Phasen (Measurement of Diffusion Rate in the Process of Dissolving Gases in Solid Phases). Zeitschrift für Phys Chemie B24:53–58

Flores-Cano JV, Leyva-Ramos R, Padilla-Ortega E, Mendoza-Barron J (2013) Adsorption of heavy metals on diatomite: Mechanism and effect of operating variables. Adsorpt Sci Technol 31:275–291. https://doi.org/10.1260/0263-6174.31.2-3.275

Furlan DM, Morgado DL, Oliveira AJAD, et al (2019) Sisal cellulose and magnetite nanoparticles: Formation and properties of magnetic hybrid films. J Mater Res Technol 8:2170–2179. https://doi.org/10.1016/j.jmrt.2019.02.005

Goodford PJ (1985) A Computational Procedure for Determining Energetically Favorable Binding Sites on Biologically Important Macromolecules. J Med Chem 28:849–857. https://doi.org/10.1021/jm00145a002

Griffin WC (1949) Classification of surface-active agents by" HLB". J Soc Cosmet Chem 1:311–326

Humphrey W, Dalke A, Schulten K (1996) VMD: Visual molecular dynamics. J Mol Graph 14:33–38. https://doi.org/10.1016/0263-7855(96)00018-5

Iqbal M, Iqbal N, Bhatti IA, et al (2016) Response surface methodology application in optimization of cadmium adsorption by shoe waste: A good option of waste mitigation by waste. Ecol Eng 88:265–275. https://doi.org/10.1016/j.ecoleng.2015.12.041

Jafari SA, Cheraghi S, Mirbakhsh M, et al (2015) Employing response surface methodology for optimization of mercury bioremediation by vibrio parahaemolyticus PG02 in coastal sediments of Bushehr, Iran. CLEAN - Soil, Air, Water 43:118–126. https://doi.org/10.1002/clen.201300616

Kaco H, Baharin KW, Zakaria S, et al (2017) Preparation and characterization of Fe3O4/regenerated cellulose membrane. Sains Malaysiana 46:623–628. https://doi.org/10.17576/jsm-2017-4604-15

Karanac M, Đolić M, Veljović Đ, et al (2018) The removal of Zn^{2+}, Pb^{2+}, and As(V) ions by lime activated fly ash and valorization of the exhausted adsorbent. Waste Manag 78:366–378. https://doi.org/10.1016/j.wasman.2018.05.052

Kardam A, Raj KR, Srivastava S, Srivastava MM (2014) Nanocellulose fibers for biosorption of cadmium, nickel, and lead ions from aqueous solution. Clean Technol Environ Policy 16:385–393. https://doi.org/10.1007/s10098-013-0634-2

Kumar R, Sharma RK (2019) Synthesis and characterization of cellulose based adsorbents for removal of Ni(II), Cu(II) and Pb(II) ions from aqueous solutions. React Funct Polym 140:82–92. https://doi.org/10.1016/j.reactfunctpolym.2019.04.014

Kundu D, Mondal SK, Banerjee T (2019) Development of β-Cyclodextrin-Cellulose/Hemicellulose-Based Hydrogels for the Removal of Cd(II) and Ni(II): Synthesis, Kinetics, and Adsorption Aspects. J Chem Eng Data 64:2601–2617. https://doi.org/10.1021/acs.jced.9b00088

Lee CG, Kim JH, Kang JK, et al (2015) Comparative analysis of fixed-bed sorption models using phosphate breakthrough curves in slag filter media. Desalin Water Treat 55:1795–1805. https://doi.org/10.1080/19443994.2014.930698

Low MJD (1960) Kinetics of Chemisorption of Gases on Solids. Chem Rev 60:267–312. https://doi.org/10.1021/cr60205a003

Lu T, Chen F (2012) Multiwfn: A multifunctional wavefunction analyzer. J Comput Chem 33:580–592. https://doi.org/10.1002/jcc.22885

M. J. Frisch, G. W. Trucks HBS et al. (2016) Gaussian 16 Revision B. 01. 2016; Gaussian Inc. Wallingford CT 46:

Mahmoud MA (2015) Kinetics and thermodynamics of aluminum oxide nanopowder as adsorbent for Fe (III) from aqueous solution. Beni-Suef Univ J Basic Appl Sci 4:142–149. https://doi.org/10.1016/j.bjbas.2015.05.008

Manning BA, Fendorf SE, Goldberg S (1998) Surface structures and stability of arsenic(III) on goethite: Spectroscopic evidence for inner-sphere complexes. Environ Sci Technol 32:2383–2388. https://doi.org/10.1021/es9802201

Moussout H, Ahlafi H, Aazza M, Maghat H (2018) Critical of linear and nonlinear equations of pseudo-first order and pseudo-second order kinetic models. Karbala Int J Mod Sci 4:244–254. https://doi.org/10.1016/j.kijoms.2018.04.001

Najib N, Christodoulatos C (2019) Removal of arsenic using functionalized cellulose nanofibrils from aqueous solutions. J Hazard Mater 256–266. https://doi.org/10.1016/j.jhazmat.2018.12.067

Olguín MT, López-González H, Serrano-Gómez J (2013) Hexavalent chromium removal from aqueous solutions by Fe-modified peanut husk. Water Air Soil Pollut 224:. https://doi.org/10.1007/s11270-013-1654-6

Pakade VE, Ntuli TD, Ofomaja AE (2017) Biosorption of hexavalent chromium from aqueous solutions by Macadamia nutshell powder. Appl Water Sci 7:3015–3030. https://doi.org/10.1007/s13201-016-0412-5

Pastor M, Cruciani G, Mclay I, et al (2000) GRid-INdependent Descriptors (GRIND): A Novel Class of Alignment-Independent Three-Dimensional Molecular Descriptors. 3233–3243

Pedretti A, Villa L, Vistoli G (2004) VEGA – An open platform to develop chemo-bio-informatics applications, using plug-in architecture and script programming. J Comput Aided Mol Des 18:167–173. https://doi.org/10.1023/B:JCAM.0000035186.90683.f2

Qiu H, Lv L, Pan BC, et al (2009) Critical review in adsorption kinetic models. J Zhejiang Univ Sci A 10:716–724. https://doi.org/10.1631/jzus.A0820524

Ren C, Ding X, Li W, et al (2017) Highly Efficient Adsorption of Heavy Metals onto Novel Magnetic Porous Composites Modified with Amino Groups. J Chem Eng Data 62:1865–1875. https://doi.org/10.1021/acs.jced.7b00198

Ren Z, Zhang G, Paul Chen J (2011) Adsorptive removal of arsenic from water by an iron-zirconium binary oxide adsorbent. J Colloid Interface Sci 358:230–237. https://doi.org/10.1016/j.jcis.2011.01.013

Rout PR, Bhunia P, Dash RR (2015) Effective utilization of a sponge iron industry by-product for phosphate removal from aqueous solution: A statistical and kinetic modelling approach. J Taiwan Inst Chem Eng 46:98–108. https://doi.org/10.1016/j.jtice.2014.09.006

Rusmirovic JD, Obradovic N, Perendija J, et al (2019) Controllable synthesis of Fe 3 O 4 -wollastonite adsorbents for efficient heavy metal ions/oxyanions removal. Environ Sci Pollut Res 26:12379–12398. https://doi.org/10.1007/s11356-019-04625-0

Saha B, Gill RJ, Bailey DG, et al (2004) Sorption of Cr(VI) from aqueous solution by Amberlite XAD-7 resin impregnated with Aliquat 336. React Funct Polym 60:223–244. https://doi.org/10.1016/j.reactfunctpolym.2004.03.003

Sellaoui L, Bouzid M, Duclaux L, et al (2016a) Binary adsorption isotherms of two ionic liquids and ibuprofen on an activated carbon cloth: simulation and interpretations using a statistical and COSMO-RS models. RSC Adv 6:67701–67714. https://doi.org/10.1039/C6RA03405E

Sellaoui L, Dotto GL, Goncalves JO, et al (2016b) Equilibrium modeling of single and binary adsorption of Food Yellow 4 and Food Blue 2 on modified chitosan using a statistical physics theory: new microscopic interpretations. J Mol Liq 222:151–158. https://doi.org/10.1016/j.molliq.2016.07.005

Serin B, Ellickson RT (1941) Determination of Diffusion Coefficients. J Chem Phys 9:742. https://doi.org/10.1063/1.1750834

Sharma S, Balasubramanian K, Arora R (2016) Adsorption of arsenic (V) ions onto cellulosic-ferric oxide system: kinetics and isotherm studies. Desalin Water Treat 57:9420–9436. https://doi.org/10.1080/19443994.2015.1042066

Sherman DM, Randall SR (2003) Surface complexation of arsenic(V) to iron(III) (hydr)oxides: structural mechanism from ab initio molecular geometries and EXAFS spectroscopy. Geochim Cosmochim Acta 67:4223–4230. https://doi.org/10.1016/S0016-7037(03)00237-0

Soldatkina L, Zavrichko M (2018) Equilibrium, Kinetic, and Thermodynamic Studies of Anionic Dyes Adsorption on Corn Stalks Modified by Cetylpyridinium Bromide. Colloids and Interfaces 3:4. https://doi.org/10.3390/colloids3010004

Stewart JJP (2013) Optimization of parameters for semiempirical methods VI: More modifications to the NDDO approximations and re-optimization of parameters. J Mol Model 19:1–32. https://doi.org/10.1007/s00894-012-1667-x

Stewart JJP (1990) MOPAC: A semiempirical molecular orbital program. J Comput Aided Mol Des 4:1–105. https://doi.org/10.1007/BF00128336

Sun N, Swatloski RP, Maxim ML, et al (2008) Magnetite-embedded cellulose fibers prepared from ionic liquid. J Mater Chem 18:283–299. https://doi.org/10.1039/b713194a

Sun X, Yang L, Li Q, et al (2014) Amino-functionalized magnetic cellulose nanocomposite as adsorbent for removal of Cr(VI): Synthesis and adsorption studies. Chem Eng J 241:175–183. https://doi.org/10.1016/j.cej.2013.12.051

Tabatabaeefar A, Yuan Q, Salehpour A, Rajabi-Hamane M (2019) Batch adsorption of lead (II) from aqueous solution onto novel polyoxyethylene sorbitan monooleate/ethyl cellulose microfiber adsorbent: Kinetic, isotherm and thermodynamic studies. Sep Sci Technol 0:1–11. https://doi.org/10.1080/01496395.2019.1581218

Taleb K, Markovski J, Veličković Z, et al (2016) Arsenic removal by magnetite-loaded amino modified nano/microcellulose adsorbents: Effect of functionalization and media size. Arab J Chem Article in: https://doi.org/10.1016/j.arabjc.2016.08.006

Vadakkekara GJ, Thomas S, Nair CPR (2019) Maleic acid modified cellulose for scavenging lead from water. Int J Biol Macromol 129:293–304. https://doi.org/10.1016/j.ijbiomac.2019.02.037

Veličković Z, Vuković GD, Marinković AD, et al (2012) Adsorption of arsenate on iron(III) oxide coated ethylenediamine functionalized multiwall carbon nanotubes. Chem Eng J 181–182:174–181. https://doi.org/10.1016/j.cej.2011.11.052

Viegas RMC, Campinas M, Costa H, Rosa MJ (2014) How do the HSDM and Boyd's model compare for estimating intraparticle diffusion coefficients in adsorption processes. Adsorption 20:737–746. https://doi.org/10.1007/s10450-014-9617-9

Voisin H, Bergström L, Liu P, Mathew AP (2017) Nanocellulose-based materials for water purification. Nanomaterials 7:. https://doi.org/10.3390/nano7030057

Witek-Krowiak A, Chojnacka K, Podstawczyk D, et al (2014) Application of response surface methodology and artificial neural network methods in modelling and optimization of biosorption process. Bioresour Technol 160:150–160. https://doi.org/10.1016/j.biortech.2014.01.021

Yu X, Tong S, Ge M, et al (2013) Adsorption of heavy metal ions from aqueous solution by carboxylated cellulose nanocrystals. J Environ Sci 25:933–943. https://doi.org/10.1016/S1001-0742(12)60145-4